Universidad Nacional Autónoma de México
Posgrado en Ciencia e Ingeniería de Materiales

Instituto de Investigación en Materiales

Synthesis and characterization of monodispersed iridium in titanium oxide

TESIS

Para optar por el grado en Maestría en Ciencia e Ingeniería de Materiales

Presenta

LSMC. Mariana Molina Torres

Tutor principal

Dr. Rubén Mendoza Cruz
Instituto de Investigación en Materiales

Comité Tutor

Dr. Rodolfo Zanella Specia
Instituto de Ciencias Aplicadas y Tecnología, UNAM

Dr. Orlando Hernández Cristóbal
Escuela Nacional de Estudios Superiores Morelia, UNAM

Ciudad de México, 2023

Universidad Nacional Autónoma de México
UNAM
Biblioteca Central
Dirección General de Bibliotecas de la UNAM

UNAM – Dirección General de Bibliotecas
Tesis Digitales
Restricciones de uso

DERECHOS RESERVADOS ©
PROHIBIDA SU REPRODUCCIÓN TOTAL O PARCIAL

Todo el material contenido en esta tesis esta protegido por la Ley Federal del Derecho de Autor (LFDA) de los Estados Unidos Mexicanos (México).

El uso de imágenes, fragmentos de videos, y demás material que sea objeto de protección de los derechos de autor, será exclusivamente para fines educativos e informativos y deberá citar la fuente donde la obtuvo mencionando el autor o autores. Cualquier uso distinto como el lucro, reproducción, edición o modificación, será perseguido y sancionado por el respectivo titular de los Derechos de Autor.

PROTESTA UNIVERSITARIA DE INTEGRIDAD Y HONESTIDAD ACADÉMICA Y PROFESIONAL
(Graduación con trabajo escrito)

De conformidad con lo dispuesto en los artículos 87, fracción V, del Estatuto General, 68, primer párrafo, del Reglamento General de Estudios Universitarios y 26, fracción I, y 35 del Reglamento General de Exámenes, me comprometo en todo tiempo a honrar a la Institución y a cumplir con los principios establecidos en el Código de Ética de la Universidad Nacional Autónoma de México, especialmente con los de integridad y honestidad académica.

De acuerdo con lo anterior, manifiesto que el trabajo escrito titulado:

Synthesis and characterization of iridium monodispersed in titanium oxide

que presenté para obtener el grado de -----Maestria----- es original, de mi autoría y lo realicé con el rigor metodológico exigido por mi programa de posgrado, citando las fuentes de ideas, textos, imágenes, gráficos u otro tipo de obras empleadas para su desarrollo.

En consecuencia, acepto que la falta de cumplimiento de las disposiciones reglamentarias y normativas de la Universidad, en particular las ya referidas en el Código de Ética, llevará a la nulidad de los actos de carácter académico administrativo del proceso de graduación.

Atentamente

Mariana Molina Torres
312015581

(Nombre, firma y Número de cuenta de la persona alumna)

Declaration of Authorship

I, Mariana Molina Torres, declare that the thesis entitled "Synthesis and Characterization of Monodispersed Iridium in Titanium Oxide" and the work presented therein are my own original work.

By means of this statement, I certify that the work carried out during the period of my Master's studies in the Postgraduate Program in Science and Engineering of Materials (PCeIM) at the Autonomous University of Mexico (UNAM) was completed in its entirety.

Furthermore, I declare that no part of this work has been used to obtain any degree or certification from UNAM or any other institution. It is worth mentioning that all resources consulted and utilized in this research have been properly attributed to their respective authors.

Whenever material created by other authors has been used, the proper reference to the original source has always been provided. With the exception of these citations, all the content presented in this work is of my own authorship.

Moreover, I have acknowledged and cited all bibliographic sources used during the development of this research. In the case of collaborative works with others, the individual contributions of each collaborator have been clearly specified.

Through this declaration, I reaffirm the academic and ethical integrity with which this research has been conducted, and I guarantee that the principles of intellectual honesty and appropriate attribution have been followed at all times.

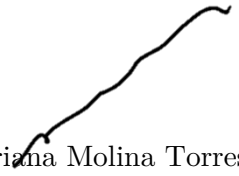

Mariana Molina Torres

Rubén Mendoza Cruz

A octubre de 2023

Intentionally blank page

Declaración de Autoría

Yo Mariana Molina Torres hago constar que la tesis titulada **Synthesis and characterization of monodispersed iridium in titanium oxide** y el trabajo presentado en ella es de mi autoría.

Por medio de la presente, certifico que el trabajo realizado durante el período de mis estudios de Maestría en el Posgrado en Ciencia e Ingeniería de Materiales (PCeIM) en la Universidad Autónoma de México (UNAM) fue llevado a cabo de manera completa.

Asimismo, declaro que ninguna parte de este trabajo ha sido utilizada para obtener algún grado o certificación de la UNAM ni de ninguna otra institución. Cabe mencionar que todos los recursos consultados y utilizados en esta investigación están debidamente atribuidos a sus respectivos autores.

Cuando se ha hecho uso de material creado por otros autores, siempre se ha proporcionado la debida referencia a la fuente original. A excepción de estas citas, todo el contenido presentado en este trabajo es de mi propia autoría.

Afirmo que el material presentado no se encuentra protegido por derechos de autor y me hago responsable de cualquier reclamo relacionado con la violación de derechos de autor. Hago constar que el trabajo que presentes de mi autoría y que todas las ideas, citas textuales, graficas, etc., sacados de cualquier obra o debidas al trabajo de terceros, han sido debidamente identificados y citados en el cuerpo del texto y en la bibliografía.

Mediante la presente declaración, reafirmo la integridad académica y ética con la que se ha llevado a cabo esta investigación y garantizo que se han seguido los principios de honestidad intelectual y atribución adecuada en todo momento.

Mariana Molina Torres

Rubén Mendoza Cruz

A octubre de 2023

Intentionally blank page

Institutional Acknowledgments

I am grateful to the National Autonomous University of Mexico for shaping me and providing me with opportunities to grow. To the Institute of Materials (IIM), I extend my thanks for the space, allowing me to study in its facilities, laboratories, and among its people.

My gratitude to the Scholarships Program of the National Council for Humanities, Sciences, and Technologies CONAHCyT for providing me with the scholarship to pursue my Master's studies CVU 1147286.

I also express my gratitude to DGAPA-PAPIIT IA106623 for providing the necessary resources to carry out my research work.

To Dr. Rubén Mendoza Cruz and Dr. Orlando Hernández Cristóbal, I express my heartfelt gratitude for their remarkable patience, unwavering dedication, and shared passion throughout this journey. Their invaluable support, the time they invested in me, and their acceptance and involvement in my project have been instrumental in its success.

I am deeply grateful for the constructive discussions that pushed me to enhance my project and for their unwavering belief in my abilities. They have not only been mentors but also catalysts for my personal and professional growth, providing me with invaluable opportunities to flourish.

To the Catalytic Reactivity Laboratory at the Institute of Physics, UNAM, I extend my gratitude, particularly to Dr. Gabriela Díaz-Guerrero for her openness, patience, and flexibility in providing me with ideas, tools, and technical support for my project. I also want to thank Dr. Antonio Gómez-Cortes for his technical support in DRIFT and TPR. Additionally, I am thankful to the laboratory technician, Pedro Huidobro García, for his human support, technical assistance, and patience throughout the project.

To the University Laboratory of Electron Microscopy (LUME@UNAM), I express my sincere gratitude, particularly to Dr. Rubén Mendoza Cruz, for his invaluable teachings, technical support, and guidance in generating and analyzing micrographs. I am also thankful to Phys. Josué Romero and Dr. Omar Novelo Peralta for his technical assistance, patience, and thorough examination of all my samples. Special thanks to Dr. Lourdes Bazán for her observations of my samples and granting me access to use the LEICA microscope.

To LAMIC, for showing me the beauty of microscopy. In particular, I am deeply grateful to Dr. Orlando Hernández-Cristóbal for teaching me with patience, love, and passion. I appreciate all the hours and discussions we had, the dedicated time to my work, and for noticing the details that I might have overlooked.

I extend my appreciation to Dr. Raul Herrera and Eng. Cristina Zorrilla for her unwavering technical support and valuable advice. I am also thankful to Samuel Tehuacanero-Cuapa for his assistance.

To Dr. Rodolfo Zanella Specia and M.S. Viridiana Maturano Rojas, I am grateful for their technical support in the CO adsorption, TPR analysis, and material reduction processes. I would also like to thank Dr. Daniel G. Araiza for his assistance in analyzing my results.

I am indebted to the personnel at IIM who have always been willing to support us, particularly M.S. Ana Karla Bobadilla for her openness in assisting me, providing technical support, and patiently teaching me how to operate the equipment. I am also grateful to Phys. Lázaro Huerta-Arcos for his technical support in XPS and for patiently guiding me through the analysis and discussions of my results. To M.S. Adriana Tejeda, I express my thanks for her technical support in DRX analysis, training in equipment usage, and her willingness to address any questions and help with my analyses. To M.S. Francisca García-López for their technical support in ICP. Special thanks to M.S. Alejandro Pompa-García for his technical support in the computing area, to Graciela Cruz Mendoza for her unwavering technical support and patience throughout and to Cain González Sánchez.

To my jury: Dr. María Beatriz de la Mora Mojica, Dr. Bertha Oliva Aguilar Reyes, Dr. María del Carmen Ortiz Cervantes, Dr. Raúl Herrera Becerra, and Dr. Rubén Mendoza Cruz, for their observations and contributions to my work.

To PAEP For awarding me the scholarship that provided me access to present my work at the POLYMAT Congress, as well as for supporting my research stay at LAMIC, and for providing the laboratory materials needed to carry out my project. Also, to Maria Luisa Resendíz for the support, for acting as the bridge between PAEP and the students, and for advocating on our behalf.

Personal Acknowledgments

A Rubén Mendoza por aceptar y creer en mi proyecto y brindarme las facilidades para llevarlo a término, por todo el apoyo y paciencia que has tenido conmigo, por exigirme y volverme a hacer las preguntas que no he respondido, gracias por tomar mi proyecto y hacerlo tuyo también.

A Orlando Hernández por ser mi guía, mi papá científico, mi soporte y amigo en esta carrera, por creer en mí y empujar mis límites siempre un poquito más. Por estar siempre siempre al pendiente de mí, gracias por escogerme para trabajar contigo, siempre ha sido un honor.

A mis padres Lulú y Enrique por apoyarme y motivarme siempre, por creer en mí, por emocionarse siempre conmigo en mis procesos y cuidar de mí; por ser las personas más bonitas que han existido.

A mis hermanos, Jacqueline, Edgar y Cris que me apoyan en todo, por acompañarme a crecer y amarme en el camino.

A Itzel por ser mi persona favorita en este mundo, por el tiempo que pasamos juntas, por cada canción, cada baile, por cuidar siempre de mí y ser mi más grande apoyo.

A mis amigos Ximena, Axel, Jasive, Eduardo, Aldo, Ale Triana, Daniel y Onchi por ser la base del amor puro e inspiración mutua, cada uno de ustedes me hace crecer, me alienta, apoya y soporta siempre, sin ustedes no había Keerani (ni Mariana), ni risas, ni llanto ni todo lo bonito que me dan. Gracias por no dejarme caer nunca.

A Mariano, por ser la sorpresa de esta vida, por creer en mí, por dejarme apoyarme en ti, por todo el amor y paciencia que me das. Estás paíchimo miamor.

A mis amigos y colegas Flor, Saret y David, que son mis personas favoritas de todo el instituto, con quien compartí toda la emoción de este viaje, todas las discusiones -y el estrés también-. Siempre fueron el apoyo y café calientito en todas esas mañanas, gracias por todas las risas y apoyo. Gracias de nuevo a Flor por cuidarme y siempre estar al pendiente de cómo voy, si me faltan trámites y también por adoptarme en tu Vallaclán, eres un sol.

Dedicatoria

A mi familia con todo el amor

Dedico este trabajo a mis padres, Lulú y Enrique, como muestra de mi profundo agradecimiento, por ser los pilares de mi esfuerzo. Por su amor y paciencia infinita, y por prepararme a la vida como lo hicieron, de manera que me dieron todas las herramientas que yo he necesitado para la vida.
Esto es gracias a ustedes. Espero que todo lo que han hecho por mi les llegue de vuelta en forma de mucho amor.

A mis sobrinos Aranza, Itziguery, Alondra, Alessandro y Andre, que este trabajo los inspire a hacer más, que mi amor y apoyo siempre va a estar con ustede

Content

Declaration of Authorship *2*

Declaración de Autoría *4*

Institutional Acknowledgments **6**

Personal Acknowledgments **8**

Dedicatoria **9**

Nomenclature *11*

Figures Index 12

1. Introduction *14*

2. General objective *16*

3.1 Specific objetives 16

3. Hypothesis *16*

4. Justification *17*

5. Background *19*

5.1 Single Atom Catalysts **19**

5.2.1 Summary of iridium as single atoms 21

5.2.2 Synthesis 23

5.2.3 Advantages and disadvantages of various synthetic approaches of SAC's 24

5.2.4 Deposition-Precipitation with Urea 26

5.2.5 Impregnation 27

6. Theoretical Background of Experimental Techniques *30*

6.1 X-Ray Diffraction 30

6.2 Temperature Programmed Reduction 32

6.3 Transmission Electron Microscopy 33

6.4 StatSTEM 39

6.5 IR / DRIFT 41

6.6 X-ray Photoelectron Spectroscopy 44

6.7 CO Oxidation 47

7. Methodology *50*

7.1 Deposition precipitation with urea 50

7.2 Impregnation 51

8. Characterization **53**

8.1 X-ray Diffraction 53

8.2 Transmission Electron Microscopy 54

8.3 Analysis of Temperature Programmed Reduction 55

8.4 CO Adsorption followed by Diffuse Reflectance 57
8.5 X-ray photoelectron spectroscopy 58
8.6 Inductively Coupled Plasma Mass Spectrometry 58

9. Catalytic Reactivity **59**
9.1 Oxidation of CO 59

10. Results and Discussion **60**
10.1 X-ray Diffraction 60
10.2 Scanning Transmission Electron Microscopy and Stat-STEM 61
10.3 Reduction Properties 75
10.4 X-ray photoelectron spectroscopy 76
10.5 Quantification 81
10.6 CO Adsorption followed by Diffuse Reflectance 82
10.6 Catalytic Reactivity 85

11. Conclusion **89**

12. Annexes **90**
12.1 Research outcomes 90

13 References ***91***

Nomenclature

ADF: Annular Dark Field
BF: Bright Field
BFP: Back focal plane
BFP: Back Focal Plane
BS: Backscattered
DPU: Deposit precipitation with urea
DRIFT: Diffuse reflectance **infrared Fourier** transform spectroscopy
HAADF: High Angle Annular Dark Field
HR/TEM: High resolution Transmission electron microscopy
ICP: Inductively Coupled Plasma Mass Spectrometry
SA: Single Atom
SACs: Single Atom Catalysts
STEM: Scanning Transmission Electron Microscopy
TCD: Thermal Conductivity Detector
TEM: Transmission Electron Microscopy
TPR: Termo programmed Reduction
XPS: X-ray Photoelectron Spectroscopy
AC-HAADF-STEM: Aberation Corrected High Angle Annular Dark Field Scanning Transmission Electron Microscopy

Figures Index

Figure 1. Nanocatalysts to Single-atom catalysts 15
Figure 2. Bragg Law 31
Figure 3. How TPR works. 32
Figure 4. TPR system 33
Figure 5 TEM and STEM 35
Figure 6 STEM detectors 36
Figure 7. STEM system and how HAADF detector collect information of atom columns.38
Figure 8. StatSTEM screen and functions 39
Figure 9 IR spectrometer adapted with a DRIFT cell. 42
Figure 10. Diffuse Reflectance on material surface 43
Figure 11. XPS system 45
Figure 12. How XPS works 46
Figure 13. Temperature Programmed Gas Chromatography 48
Figure 14. Deposition-precipitation method with urea and sample reduction. 51
Figure 15. Impregnation method for Ir/TiO2 SAC 52
Figure 16. DRX to TiO2, Ir/TiO2 -DPU and Ir/TiO2 Impregnation systems. TiO2 corresponds to rutile phase and there are no peaks related to iridium observed. 60
Figure 17. Various Ir/TiO2 systems. HAADF-STEM images of synthesis performed in this work, refer in Table 3 62
Figure 18. Zone axis of facets in TiO2 and diffraction pattern and FFT patterns 63
Figure 19. Facets of TiO2 where the facets in green are the ones that correspond to (110), the red ones to (100), the little wine one to (001) and the purple ones to (101). 64
Figure 20. HAADF-STEM to TiO2 support and StatSTEM 3D model. 65
Figure 21. Orientations of TiO2 crystal lattice 67
Figure 22. HAADF-STEM images of Ir/TiO2-DPU 74
Figure 23. HAADF-STEM of Ir/TiO2, intensity profile, SimulaTEM, and illustration 76
Figure 24. AC-HAADF-STEM measurements were employed to visually inspect the distribution of Ir in the 0.25% Ir/TiO2 catalyst. Notably, no Ir nanoclusters were observed, and some individual Ir atoms were identified as bright dots highlighted in yellow circles. 77
Figure 25. Ir/TiO2 by StatSTEM, intensity profile and analysis of Ir atoms 78
Figure 26. HAADF-STEM image of Ir/TiO2-Impregnation. 69
Figure 27. AC-HAADF-STEM measurements were employed to visually inspect the distribution of Ir in the 0.25% Ir/TiO2-Impregnation catalyst. Individual Ir atoms were identified as bright dots highlighted in yellow. 70
Figure 28. Ir/TiO2-Impregnation A) HAADF-STEM image, B) image filtered using StatSTEM, C-D) atom selection model, E) atom quantification, F-G) 3D model of surface iridium, H-I) measurements between iridium atoms dispersed on the support. 71
Figure 30. Profile reduction of temperature programmed reduction of A, M and TiO_2. 73

Figure 29 XPS survey in a) Ir/TiO_2-DPU and b)Ir/TiO_2-Impregnation 84
Figure 30. XPS Spectra of references TiO_2 a-b, c iridium Ir0 reference and samples Ir/TiO_2 deposition-precipitation d-f and Impregnation g-i. 79
Figure 31. DRIFT Spectra of Ir/TiO_2 samples with NPs and single atoms supported on TiO2. 83
Figure 32. DRIFT spectra of Ir/TiO_2-DPU. 84
Figure 33. DRIFT spectra of Ir/TiO_2 -Impregnation. 85
Figure 34. CO conversion with catalysts Ir/TiO_2-DPU and Ir/TiO_2-Impregnation activated in hydrogen. 86
Figure 35. CO references with the catalyst of study in this work 87

1. Introduction

Catalysis plays a fundamental role in influencing the way we live, over 90% of all chemical products involve at least one catalytic step in their manufacture[1]. Metal nanostructures supported on nano materials are widely employed as heterogeneous catalysts in industrial processes. Significant efforts have been directed towards improving the efficiency of these supported metal catalysts by reducing the size of the metal particles[2]. The size of metal particle is a critical factor in determining the effectiveness of the catalysts, new findings from both theoretical and experimental studies have shown that clusters with sizes smaller than a nanometer exhibit enhanced catalytic activity and/or selectivity compared to particles of nanometer-scale dimensions see **Figure 1** [3,4]. Single-atom catalysts (SACs) represent a rapidly expanding research field in catalysis with significant application potential. There have been reports indicating that active sites often correspond to low coordination sites, such as unsaturated atoms[5]. It has been observed that the activity and selectivity in various chemical reactions have improved when using SACs, for example: hydrogen production, ethene hydrogenation, oxygen evolution reaction, water-gas shift reaction, and oxidation reactions[6–10].

The significance of developing single-atom catalysts emerges as a challenge. Having uniform active sites is highly complicated, the support structure in the vicinity of the single atom (SA) introduces heterogeneity to the active sites of the SACs, perhaps better conveys that the individual metal atoms are situated on the surface of another material[11]. Is inherently challenging is maximizing atom utilization and precisely defining active centers.

In this thesis, various approaches to depositing iridium on TiO_2, their associated conditions, and the possibility of characterizing these materials structurally,

including in-depth identification of the unique iridium atoms, will be discussed. Subsequently, their catalytic reactivity will be reviewed by the oxidation of carbon monoxide that is a widely explored reaction, common in the domain of heterogeneous catalysis due to its significance in environmental preservation and fundamental research. Carbon monoxide on its own, serves as a valuable probe molecule for characterizing catalysts.[12]

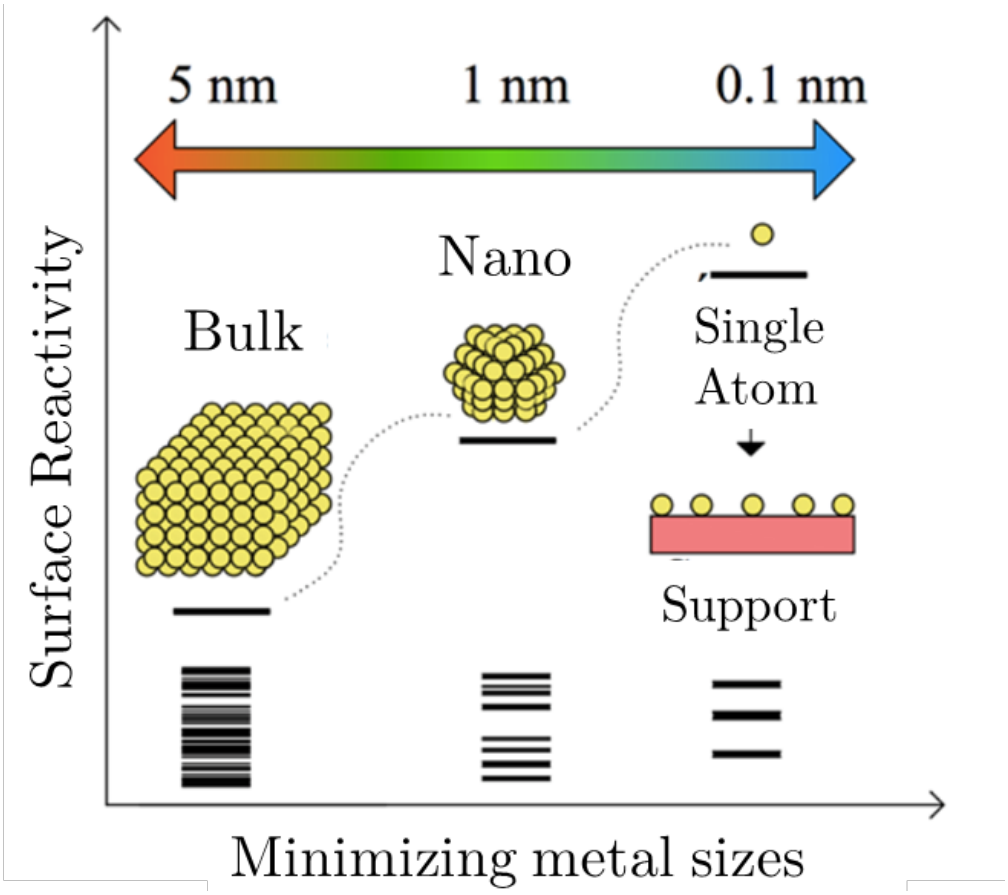

Figure 1. Nanocatalysts to Single-atom catalysts

2. General objective

To study the behavior of iridium monodispersed on titanium oxide (TiO_2), the synthesis and the detailed characterization of their structure and catalytic reactivity.

3.1 Specific objetives

I. Deposit monodispersed iridium on titanium oxide using the deposit-precipitation and impregnation method.

II. Characterize the structure of the system using advanced techniques such as HAADF-STEM and STAT-STEM simulation, in addition to XRD, TPR, DRIFT, XPS, EDS and ICP, to gain comprehensive insights into its properties, including where the iridium is located on the TiO_2 support.

III. Compare the amount of deposited iridium using both synthesis methods.

IV. Test the catalytic activity of the two systems, DPU- Ir/TiO_2, Imp- Ir/TiO_2 in the CO oxidation reaction and its correlation with previously achieved advancements in Ir/TiO_2 as NPs of iridium.

V. Compare the efficiency of both methods in order to obtain SACs from Ir in the Ir/TiO_2 system and compare the reaction yield with regarding both systems Ir/TiO_2.-DPU-Ir/TiO_2 and Imp-Ir/TiO_2 studying its catalytic activity through CO oxidation.

3. Hypothesis

• It is feasible to improve the synthesis of a catalyst with monoatomic iridium sites when using TiO_2 as a support through the techniques of deposition, precipitation, and wet chemistry.

4. Justification

The research into Ir/TiO_2 rutile catalysts is not only of great interest but also crucial for several compelling reasons. Firstly, precious metal nanoparticles, such as iridium, have gained significance due to their immense potential in catalysis.

Iridium itself is renowned for its exceptional catalytic activity, making it an ideal candidate for catalytic studies. However, in the context of single-atom catalysts (SACs), where individual atoms are dispersed on substrates, understanding the interaction between these single atoms and a metal oxide support becomes pivotal. This interaction profoundly influences the electronic structure of the catalysts, ultimately dictating the intrinsic activity of their active sites. Therefore, delving into the behavior of iridium on TiO_2 supports is essential to harness its full catalytic potential.

The research conducted by the Gates group on MgO[13] has shed light on the critical need for Sinter-Resistant Catalysts, particularly those supported by iridium. Their findings suggest that iridium at critical sizes resist aggregation, a property of paramount importance. Aggregation would require energetically unfavorable rearrangements of surface atoms, as confirmed by scanning transmission electron microscopy (STEM) images displaying the non-coalescence behavior of iridium clusters at the critical size. This resistance to aggregation is vital for ensuring the stability and effectiveness of iridium catalysts.

Furthermore, the choice of TiO_2 as a support material offers unique advantages, including its expansive surface area and exceptional stability. The rutile phase of TiO_2, specifically, has been proven to enhance the dispersion of the metal, thereby significantly improving the accessibility and reactivity of iridium species in catalytic reactions. This exceptional characteristic of the rutile phase, combined with the

advantageous properties of TiO_2 as a support, underscores its pivotal role in the development of highly efficient and selective catalytic systems. Therefore, it is not merely a matter of interest but a necessity to explore TiO_2, particularly its rutile phase, as a support material for iridium catalysts to advance the field of catalysis and address pressing environmental and industrial challenges.

5. Background

5.1 Single Atom Catalysts

Late transition metals dispersed at the atomic level are commonly known as single-atom catalysts. These catalysts feature individual isolated atoms anchored to their surfaces, driving catalytic reactions. Typically, these single atoms are distributed randomly and uncontrollably across substrates. The interaction between these single atoms and a metal oxide support can vary depending on the environment, regulating the electronic structure of the catalysts and influencing the intrinsic activity of active sites.

Single-atom catalysts can be distinguished from other related single-site catalysts, such as organometallic catalysts. In the case of organometallic catalysts, an organometallic complex is used to create the single-atom site while retaining some of its ligands to facilitate the catalytic reaction. Single-atom catalysts represent the highest level of metal dispersion on a surface, with all atoms being exposed. This is particularly crucial for expensive and scarce noble metal catalysts like Ir, Pd, and Pt, which not only find extensive applications but also attract significant interest for research purposes.**5.2** Previous work about iridium as SACs

Fabrication of SACs is hard due to the tendency of single atoms to aggregate adds an additional layer of complexity, making it an even greater challenge. Elements with extremely low abundance on Earth are often the most active in catalytic reactions. This is precisely why optimizing the utilization efficiency of metal atoms and providing a greater number of exposed sites for reaction activation are crucial factors.

Single atom catalysts (SACs) have a significant advantage in achieving 100% atomic utilization, making them a great way to reduce the amount of precious metals without sacrificing catalytic efficiency. Therefore, studying metals like atomically dispersed iridium doesn't impede the sustainable use of the metal. This exceptional property allows it to maintain its mechanical properties even at temperatures higher than 2000 °C and pressures up to 1.4 Mbar. Additionally, iridium has outstanding resistance to corrosion, making it highly suitable for a wide range of applications[14].

Precious metals from Group VIII, like Pd, Rh, Pt, and Ir, show excellent catalytic activities. When combined with a transition metal oxide support, they catalyze a variety of reactions. Iridium has a higher atomic mass compared to Pd and Rh and belongs to the group with the highest melting point. It exhibits versatile coordination chemistry, making it easy to disperse in various metal oxide supports such as MgO, FeOx, or $MgAl_2O_4$, with a robust interaction with the support [14,15]. For instance, Ir single-atom coordination with reduced Fe_2O_3, MgO, and TiO_2, corresponds to a substitutional configuration on the cation vacancies, with Ir coordinated with two oxygen atoms, which number could change after reaction[10]. A synergetic affect take place between the single atoms and their supports, lowering the reduction temperature of the support and generating a large amount of oxygen vacancies which contributes to their activity. The reducibility of the support also contributes to the stability of the single atoms, exhibiting high activity and selectivity.

Despite of this, few studies exist on Ir SACs in comparison with these other metals of the group, finding most applications in electrocatalysis.

The pioneers in the field of catalysis utilizing iridium as an active center have posited that the success in fabricating single atom catalysts with iridium may be attributed to the remarkably low loading of the metal[16]. The probability of encountering short-

range and long-range iridium-iridium interactions is estimated to be as minimal as 0.001 atoms nm^{-1}. Furthermore, upon increasing the iridium loading to 0.32%, a corresponding rise in observation frequency within the range of 0.5-1 nm was noted. Remarkably, no aggregation to sizes exceeding 1 nm was observed[17] therefore, it is advantageous to propose monodispersed iridium catalysts.

5.2.1 Summary of iridium as single atoms

There are many examples of synthesis where iridium has been used as an active metal center on various supports, where the nominal content of iridium supported was different, as the synthesis method and the application. In **Table 1**, are shown some examples where Ir was the protagonist.

Table 1 Summary of catalysts using iridium and different supports.

Single Atom	**Support**	**% wt. metal**	**Synthesis Method**	**Application**	**Ref**
Ir	ZIF-8	...	Impregnation Method	O.R.R.	[16]
Ir	FeOx	0.01%	Co-Precipitation Method	Water-Gas Shift Reaction	[18]
Ir	$MgAl_2O_4$	0.20%	Wet-Impregnation	...	[19]
Ir	ZrO_2@C	0.60%	Pyrolysis	Hydrogenation of LA to GVL	[16]

Ir	MgO	1%	Reported Method	Ethene Hydrogenation	[20]
Ir	TiO_2 Rutile	1%	Impregnation Method	Catalytic Oxidation of Ammonia	[21]
Ir	ZIF-8	1.20%	Pyrolysis	Formic Acid Oxidation	[22]
Ir	AP-POP	1.25%	Wet-Impregnation	Quasi-Homogeneous Hydrogenation Transformation of CO to Formate	[23]
Ir	H-Carbon ZIF-8	2.20%	Reported Method	O-H Carbenoid Insertion	[24]
Ir	Co_3O_4	4.20%	Solid-State	Ammonia Production	[25]
Ir	C-N	4.40%	Pyrolysis	Epoxidation of Styrene	[26]
Ir	Cobalt Oxide	4.93%	Surfactant-Mediated Method	O.E.R.	[27]
Ir	NiO-CC	18%	Wet Immersion	O.E.R.	[28]
Ir	N-C	40%	Pyrolysis	Electrochemical CO_2 Reduction	[29]

Summary of catalysts using iridium and different supports.

Currently, there is ongoing research into synthesis methodologies aimed at creating SACs, with wet impregnation being identified as the most promising approach. Although wet impregnation offers simplicity and scalability, it is important to acknowledge certain limitations. These include the challenge of achieving optimal metal loading and precise control over the anchoring position of isolated metal species on substrates, which can impact both catalytic efficiency and the feasibility of practical industrial applications.

5.2.2 Synthesis

The exploration and development of synthetic methodologies for single atom catalysts have become one of the most crucial research focuses. Fabricating single atom catalysts and maintaining the atomic dispersion of metal species under realistic synthesis and reaction conditions pose significant challenges. From a practical perspective, an alternative and preferable approach is the development of wet-chemistry synthetic methods for single atom catalysts (SACs)[29]. This approach provides straightforward operation and the possibility for extensive manufacturing. In wet-chemistry synthesis, mononuclear metal species are commonly employed as starting materials. Therefore, incorporating synthetic approaches to achieve the separation and isolation of the precursor at the atomic level, while also preventing the migration and agglomeration of the formed single atoms, becomes essential for the successful synthesis of Single Atom Catalysts (SACs). These factors are pivotal in guaranteeing the effective and controlled production of SACs.[29]. Ir precursors are deposited onto the substrate surface using various wet-chemistry methods. This includes dispersing metal precursors onto substrates through deposition-precipitation, coprecipitation, or wet-impregnation methods. Following this, reduction or activation procedures are undertaken to create catalysts based on Ir

with Ir species dispersed at the atomic level. These processes are vital for attaining the intended dispersion and isolation of individual Ir atoms on the substrate, facilitating the synthesis of exceptionally effective catalysts with distinctive properties and reactivity[30].

5.2.3 Advantages and disadvantages of various synthetic approaches of SAC's

The synthesis of SACs is relatively new, so techniques that have been used for nanocatalysts have also been applied. In **Table 2**, some advantages and disadvantages of various synthesis methods for obtaining SACs are presented[30].

Table 2 From [31] presents a detailed comparison of different synthetic strategies, offering a comprehensive overview of their individual advantages and disadvantages in a concise and organized manner.

Synthetic Strategy	**Advantages**	**Disadvantages**
Pyrolysis	Simple procedure, utilization of inexpensive raw materials, potential for large-scale production	High temperature, agglomeration of isolated metal atoms, uncontrollable metal sites on substrates
Electrochemical deposition	Simple procedure, controllable metal loading content	Uneven dispersion of isolated metal atoms, limitation of chemical environment and thermodynamic control
Photochemical reduction	Cost-effective procedure, no requirement for extra chemical or physical treatment, controllable nucleation	Limitation to specific systems, narrow applicability, sluggish nucleation growth rate

Atomic Layer deposition	Controllable metal-loading content, structure-performance exploration, Excellent deposition uniformity and reproducibility. The loading of the singly dispersed atoms could be adjusted via regulating the number of cycles	High-cost equipment, slow synthetic process, high vacuum conditions, uncontrollable thickness and loading content, Only materials with suitable ligands or functional groups could be chosen as support Not applicable for the commercial preparation
Wet chemical	Simple procedure, low cost, easily scalable	Low metal loading, difficulty in managing metal atoms on substrates, strong dependence on synthesis factors
Atom trapping method	Simple approach, practical method	High synthesis temperatures, requires a supply of mobile atoms and a support that can trap the mobile species
Two-step doping method	easy creation of vacancies on support and the high binding energies between the dopant and the vacancies, highly stable SACs	Limited to graphene
Ball-milling method	Convert reactants into products during the reaction process, scale-up production, green	Not uniform sites, Requires high energy atom/ion generator,
Photoreduction method	no special equipment is needed, easy to implement	Catalytic active center generally is not uniform

In situ methods	Simple procedure, high dispersion, no metal loss	Limitation to specific systems, few references to a variety of metals

Bringing up the fact that there's not much metal used might seem like a downside, but for single-atom catalysts (SACs), it's a big plus since it means less use of expensive metals. And it's also worth noting that these processes can be scaled up for larger production.

5.2.4 Deposition-Precipitation with Urea

Deposition-precipitation is a frequently used method in catalyst preparation. It involves placing metal precursors onto a supporting material and then precipitating the metal species with the help of a precipitating agent. This method allows for accurate and consistent dispersion of the metal species on the support, resulting in catalysts with well-defined structures and characteristics. Deposition-precipitation offers advantages such as easy scalability, versatility, and the ability to tailor the catalyst composition by adjusting the deposition and precipitation conditions[32,33].

The deposition-precipitation technique has been widely used to fabricate gold catalysts in Haruata working team[34,35]. In this approach, the pH of an aqueous solution containing $HAuCl_4$ is meticulously modified within the range of 6 to 10, while considering the isoelectric points of the metal oxide supports. This pH adjustment is vital because of the amphoteric nature of $Au(OH)_3$, guaranteeing the creation of durable and evenly spread gold species on the support material. The Deposition-Precipitation (DP) method is user-friendly and grants authority over the composition and characteristics of the catalyst, rendering it a favored option in industrial catalyst manufacturing[34–36].

5.2.5 Impregnation

The impregnation method is a practical technique utilized to introduce an active compound into a porous surface or support. This procedure involves immersing the support in a solution containing the active compound, permitting its absorption into the porous surface. After impregnation, the support undergoes drying or thermal treatment to remove the solvent and affix the active compound to the support. This method provides significant flexibility, allowing for control over the quantity of the active compound loaded and the fine-tuning of catalyst properties to meet specific application requirements. It is widely employed in catalyst synthesis, particularly in the development of supported catalysts on porous materials[37].

Support materials play a crucial role in the stability and catalytic performance of single-atom catalysts. These catalysts heavily rely on the support to provide a solid foundation for the deposition of active metal species. The choice of an appropriate support is of paramount importance as it directly influences the dispersion, accessibility, and reactivity of the active sites. Additionally, the support acts as a vital stabilizing agent, preventing the coalescence or aggregation of individual metal atoms and ensuring their sustained single-atom state during catalytic reactions. By offering a substantial surface area for the immobilization of metal atoms, the support facilitates efficient interactions with reactants, thereby enhancing catalytic reactions. Thus, meticulous selection and thoughtful design of suitable support materials are indispensable for the successful utilization of single-atom catalysts in diverse catalytic applications.

Titanium is a metallic element that occupies the 22nd position in the periodic table. It is highly abundant in the Earth's crust and exists in three main crystal forms: anatase, rutile, and brookite. Titanium is known for its exceptional strength-to-

weight ratio, corrosion resistance, biocompatibility, affordability, and eco-friendliness[38]. These properties make it a valuable material in various industries, as it offers a cost-effective and environmentally friendly solution. Titanium also serves a significant role in catalysis. TiO_2 are employed both as supports for catalysts and as catalysts themselves. These catalysts, including metal/TiO_2 and metal oxide/TiO_2 composites, play a significant role in diverse reactions such as hydrogenations, hydrodesulfurizations, selective oxidations, reductions, and Fischer-Tropsch processes. An additional notable feature lies in its capacity as a photocatalyst, which stems from its inherent semiconducting properties[39,40].

The careful choice of a catalyst support plays a vital role in promoting the even distribution of active components and fine-tuning catalytic functions via metal-support interactions. The catalyst support plays a pivotal role in shaping the overall performance and durability of the catalyst system, enabling enhanced regulation of reaction rates and selectivity. It functions as a foundation, aiding in the secure attachment and even dispersion of active species, thus creating a stable environment for catalytic reactions.[41]. The interaction between metal/TiO_2 has been studied as SMSI effect. The finding of heteroatomic metal-metal bonding suggested that titanium cations at surfaces might be capable of bonding to metal cations or metal atoms in a supported phase due to of the possibility of an interaction between the d orbital electrons of the surface cations and those of the supported metal atoms[42].

As mentioned earlier, various supports like MgO, ZIF-8, and Al_2O_3 have received extensive attention in the literature for their use in supporting iridium catalysts. Notably, titanium dioxide (TiO_2) has not been the favored choice as a support material, thus creating an opportunity for further investigation. TiO_2 offers notable advantages, including its expansive surface area and robust stability. Furthermore,

the utilization of the rutile phase of TiO_2 has demonstrated an enhanced capacity for dispersing the metal in comparison to other phases. The rutile phase establishes a conducive environment for the dispersion of iridium species[43]. Enhancing their accessibility and reactivity in catalytic reactions is key. The distinctive attribute of the rutile phase, when coupled with the favorable properties of TiO2 as a support, positions it as a promising contender for supporting iridium catalysts. Delving into the potential of TiO_2, specifically its rutile phase, as a support material for iridium catalysts, offers significant potential for the advancement of exceptionally efficient and selective catalytic systems.

6. Theoretical Background of Experimental Techniques

6.1 X-Ray Diffraction

X-ray diffraction crystallography is a well-established and extensively applied technique in the realm of materials analysis. It is utilized to glean insights into the atomic-level structure of diverse materials in different states, specifically composition, crystal structure, and crystalline grain size of materials. There have been numerous advancements in this field, building upon the pioneering work of Max von Laue in 1912 and W.L. Bragg and W.H. Bragg in 1913, who first discovered X-ray diffraction from crystals.

In X-ray diffraction, we utilize the diffraction of electrons, neutrons, and protons through a crystal. The diffraction is dependent on both the crystal structure and the wavelength. An X-ray beam is an electromagnetic wave distinguished by a consistent-frequency electric field oscillation, oriented perpendicular to its direction of propagation. Owing to the electron's recurring cycles of acceleration and deceleration, a novel electromagnetic wave, commonly recognized as X-rays, is emitted. The phenomenon of diffraction, with respect to the atomic position, occurs when an X-ray beam interacts with a crystal possessing a regularly repeating atomic structure over a long distance. The magnitude of diffracted X-ray intensity is contingent not only upon the atomic structural arrangement but also on the identity of the atomic species[44].

The diffracted beams originating from a crystal occur due to a simple but compelling Bragg explanation, which is validated primarily because it yields the accurate outcome. Imagine that the incoming waves are specularly bounced off parallel layers of atoms within the crystal, where each layer reflects only a tiny portion of the radiation, resembling a sparsely mirrored surface. In specular, mirror-like reflection,

the angle at which the waves approach equals the angle at which they bounce off. The diffracted beams emerge when the reflections from these parallel atomic layers combine constructively. We are addressing the phenomenon of elastic scattering, wherein the energy of the incident X-ray remains unchanged upon reflection. Consider a scenario involving parallel lattice planes spaced at a distance 'd.' The incident X-ray radiation is directed within the plane of the medium. The variation in path length for rays reflected from adjacent planes can be expressed as 2d sin(θ), where "θ" represents the angle measured from the plane. Constructive interference of radiation emanating from successive planes occurs when the path difference equates to an integer value "n" of wavelengths (λ). The diffracted X-rays originating from every atom within the crystal lattice planes are meticulously synchronized in phase, leading to the generation of a diffracted X-ray beam of substantial intensity in a specific direction that conforms to the Bragg law equation.

$$2dsin\theta = n\lambda$$

In this context, "n" is denoted as the order of reflection, representing the number of wavelengths encompassed within the path difference between diffracted X-rays from adjacent crystal planes see **Figure 2**. The Bragg law is an outcome resulting from the intrinsic periodicity of the lattice structure. [45,46]

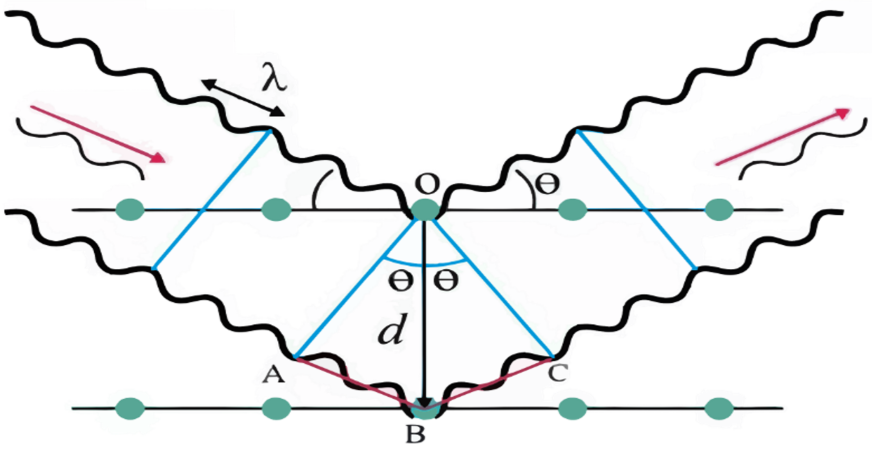

Figure 2. Bragg Law

6.2 Temperature Programmed Reduction

Programmed temperature reduction is a characterization technique primarily oriented toward the examination of metal oxides and metal oxides dispersed on a supporting substrate. The procedure entails the continuous flow of a gas, functioning as a reducing agent, through the solid material targeted for reduction while simultaneously subjecting it to a linear temperature increase over time [47]see **Figure 3**.

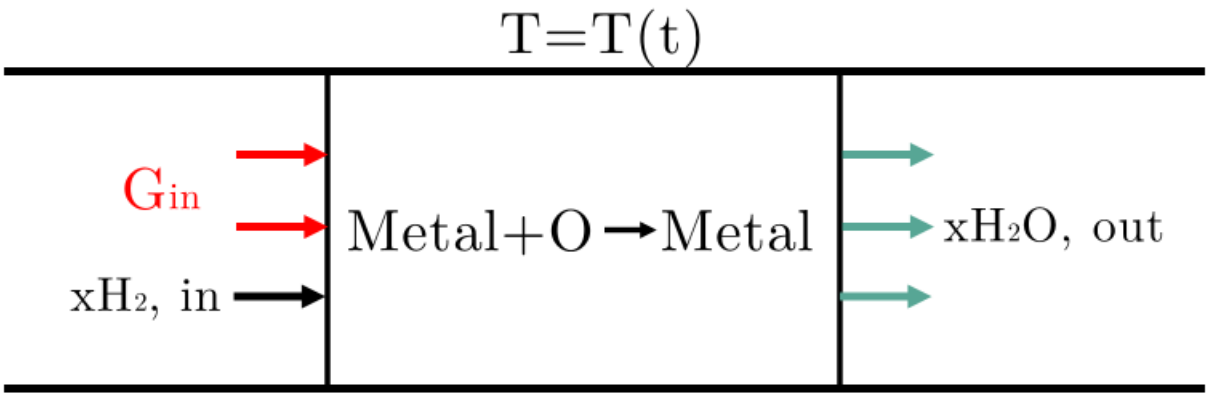

Figure 3. How TPR works. The H_2 gas is introduced into the system to come into contact with the material containing the metal and carry out its oxidation.

Programmed temperature reduction, employing hydrogen (hydrogen diluted with an inert gas) as the reducing agent, recognized as TPR-H_2, finds extensive application in the characterization of catalysts in the forms of oxides or precursors to the active phase. The reduction rate is perpetually monitored by quantifying the composition (H_2 content) of the gaseous mixture at the reactor outlet through a thermal conductivity detector (TCD) see **Figure 3**. The process can transpire in a single or multiple stages, as evidenced by the consumption of hydrogen, and culminates when the material is partially or completely reduced. The reduction reaction of a metal oxide can be denoted by Equation, where 'M' represents a transition metal: [48]

$$MO(s) + H_2(g) \longrightarrow M^0(s) + H_2O(g)$$

TPR analysis serves to quantify the volume of H_2 absorbed by the material to know the reduction properties of a material by which metallic precursors are reduced. These assessments are conducted utilizing a thermal conductivity detector (TCD), where the count of reducible species gradually diminishes as the temperature is meticulously controlled and incrementally elevated. TPR experiments yield thermograms, which depict a reduction profile consisting of one or more peaks, indicative of the material's reduction process. [47] The area encompassed beneath the curve effectively represents the extent of hydrogen consumption during the reaction.

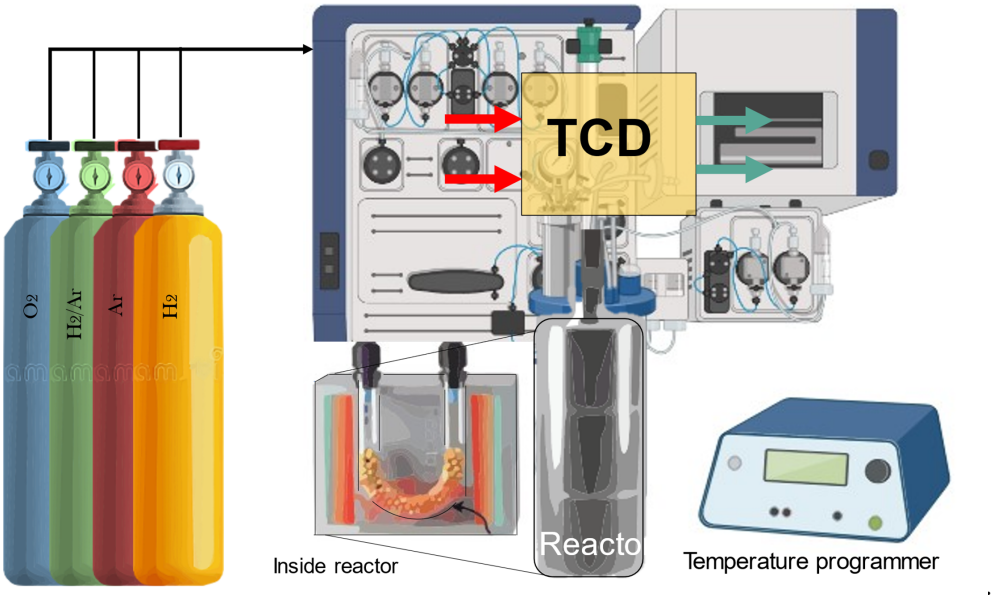

Figure 4. TPR system where the different gases connected to the TPR are observed, the reactor is shown in which, inside it, the reaction takes place. This equipment is associated with a temperature controller and its computer.

6.3 Transmission Electron Microscopy

Transmission electron microscopy (TEM) is an advanced characterization method that employs a focused and accelerated beam of electrons to acquire detailed and high-resolution images of specimens at the micro and nanoscale. By passing the

electron beam through a less than 200 nm of thickness specimen, TEM can yield valuable insights into the internal structure, composition, and morphology of the sample. This technique relies on the interaction between electrons with atoms within the sample, resulting in signals that are captured by detectors and transformed into images.

A transmission electron microscope (TEM) includes a collection of lenses and condenser apertures, see **Figure 5** the components of a traditional TEM microscope. It features an electron source, where electrons are drawn and accelerated through the application of a voltage difference; this procedure is known as field emission. The field emission system consists of a ZrO/W emission cathode, featuring a semi-spherical cathode tip with an approximate radius of 0.1 micrometer. The anode applies a spherically symmetric voltage, creating a spherical capacitor that generates an electric field described as:

$$E \propto (V/r)$$

When r is extremely small and potential differences are low, a substantial electric field is generated, assisting in overcoming the potential barrier of ZrO/W to extract its electrons. Following this, the electron emission system, along with apertures and condenser lenses, illuminates the sample with electrons.

Within the realm of TEM, two primary transmission modes exist: conventional TEM and scanning transmission electron microscopy (STEM). Both TEM and STEM instruments produce transmission electron images, but there are differences between these imaging modes.

In conventional TEM, an image is produced on a screen where pixels are observed simultaneously, and image magnification is controlled by the projector lenses after the electron beam has passed through the sample. In STEM mode, the signal is measured using one or more electron detectors, resulting in an image that is

progressively constructed, point by point. The convergence in STEM is different from TEM, as the beam in TEM is often converged to a spot on the specimen.

STEM can be used to create diffraction contrast images, which also affect the appearance of diffraction patterns. The highly convergent probe in STEM images can be seen as if the beam is scanning and recording the electron paths in the microscope column, capturing the diffraction pattern from a small region of the sample. However, STEM instruments are not primarily used as diffraction instruments.

In terms of instrument geometry, STEM does not require projector lenses after the specimen, and the post-specimen space in STEM can be utilized to accommodate multiple electron detectors[49].

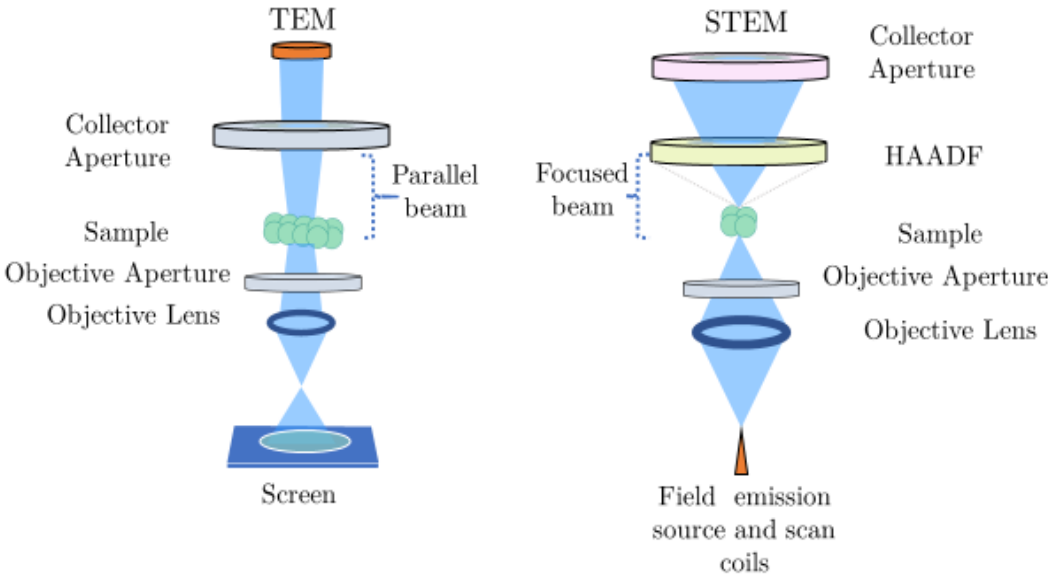

Figure 5. TEM and STEM systems.

STEM and TEM represent formidable tools extensively applied in the field of catalysis research. One of the standout characteristics of these methods is their capacity to rectify spherical aberration, enabling the acquisition of high-resolution images at the atomic level. Thanks to the emergence of cutting-edge electron

microscopy devices, aberration-corrected STEM provides the means to observe individual atoms and atomic configurations within catalyst materials. Such an exceptional level of precision proves particularly invaluable when investigating single-atom catalysts (SACs), as the distribution and configuration of individual metal atoms significantly influence their catalytic effectiveness.

Transmitted electrons and detectors

All the electrons scattered during the process can be captured using various detectors positioned behind the sample see **Figure 6**, and their data can be fully utilized.

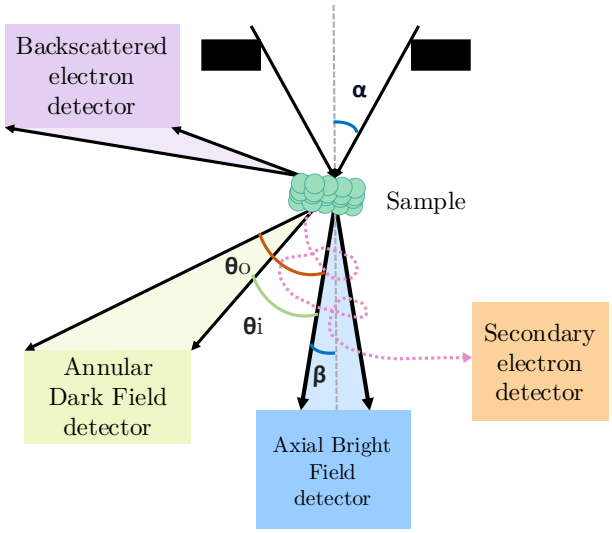

Figure 6. STEM detectors

Bright Field (BF): This detector is used to detect electrons transmitted at relatively low angles with respect the incident beam axis, the BF detector is aligned with the axis and typically has a β value of around 1-15 mrad. Its definition is determined by the collector aperture size and potential post-specimen lens effects.

Annular Dark Field (ADF): If the electrons transmitted at relatively high angles its posible to use an ADF detector. In this case, the inner hole of the detector is intentionally positioned to narrowly miss collecting electrons from the outer edges of

the probe envelope. This usually occurs within an angular range of θ_1-θ_0 ≈15-50 mrad. Dark field imaging is particularly relevant because is used to collect the signal that produce the imagethat depend almost on the individual contribution of the atoms present on the sample. The dependance on Z is remarked at high angles (50mrad)

High Angle Annular Dark Field (HAADF): With a larger inner hole diameter, this detector allows the most highly diffracted beams to pass through. Typically, this occurs within an angular range of θ_1-θ_0 ≈ 50-150 mrad. One of the most interesting propierties of the HAADF is the dependence of the signal with the thickness and with the atomic number thas goes as:

$$Z^{1.7}$$

STEM-HAADF is also known as Z-contrast image. The benefit of this technique is that it allows relatively simple image interpretation to a good approximation. In many cases, the bright spots on a Z-contrast image correspond to the positions of the atoms, and spot intensity is related to atomic number in a readily understandable manner. Therefore, finding atomic positions depends on locating local maxima, and image intensity provides clues about the number of atoms and their atomic numbers.

Secondary Electron (SE): These are low-energy electrons that are collected without having a direct line of sight to the sample. Specific angles are not typically reported.[49].

High resolution STEM experiments are distinguished from conventional plane wave TEM experiments by the small dimensions of the converged electron prove, wich is able to reach sizes bellow atomic bond lenghts with modern aberration-correction technology, that is the key advance in modern microscopy.

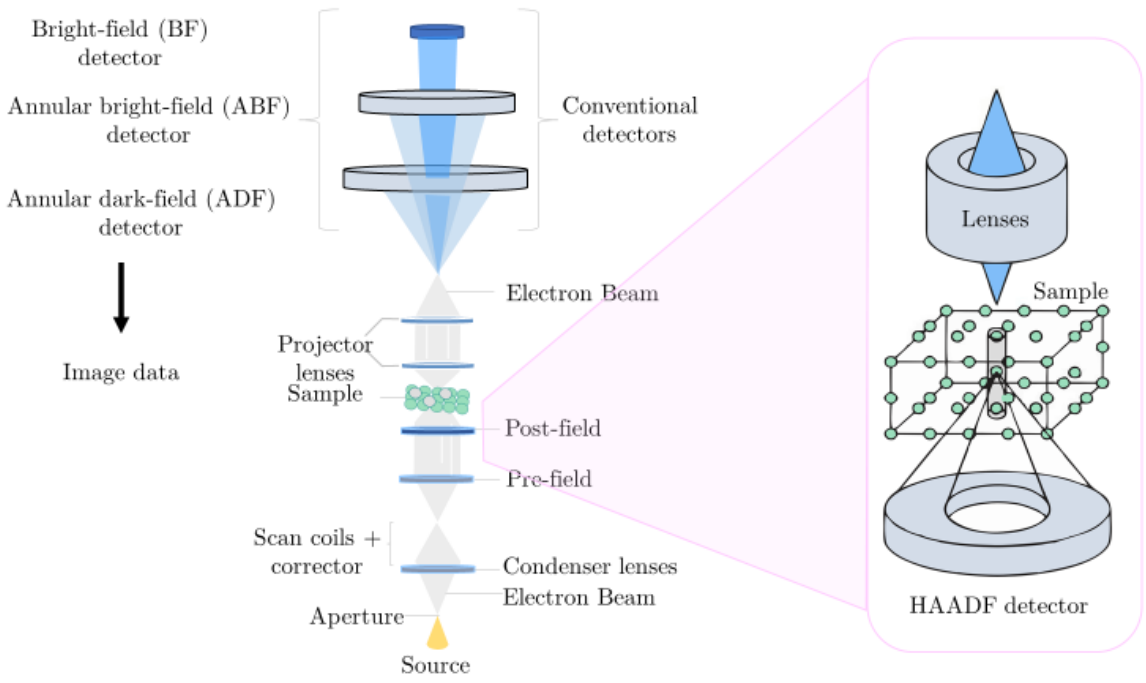

Figure 7. STEM system and how HAADF detector collect information of atom columns.

To observe isolated atoms, it is necessary to work with a TEM equipped with a spherical aberration corrector Cs. In a spherical-aberration corrected probe can be compensated by a slight negative C_3[59]. The optimal resolution for an uncorrected system can be expressed as:

$$d_{opt} = 0.43\lambda^{3/4}C_3^{1/4}$$

and for a *Cs* corrected system, the limiting resolution due to the n^{th} order aberration:

$$d_{opt} = 0.45\lambda^{5/6}C_3^{1/6}$$

In a 200 keV aberration-corrected microscope, C3 can be adjusted to positive or negative values close to zero, whereas for an uncorrected high-resolution microscope, C3 is approximately 0.5 mm. The electron probe diameter in STEM can be minimized through the aberration-corrected system, which incorporates a hexapole corrector with two multipole stages, compensating for all aberrations up to the 3rd order[57]. Next, the petite probe is traversed across the sample, engaging with its atoms, resulting in an arrangement of distinct scatters. Presently, the intensely convergent

electron beam engages individually with each scatter (in contrast to a broad parallel beam interacting with numerous scatters in TEM). Each atom, portrayed as a potential spike, scatters in correlation with the local probe intensity. Hence, the image's intensity can be articulated as:

$$I(r) = O(r) \otimes |P(r)|^2$$

In other words, the image intensity is the convolution of the object O(r) (an array of scatters) and the probe intensity profile P(r). The sharper the probe, the more distinctly the atoms are visible.[53]

6.4 StatSTEM

The properties of nanoparticles are influenced by their three-dimensional (3D) morphology, structure, and composition. StatSTEM is a tool that hepls the characterization techniques to determine the arrangement of all atoms in 3D. Atom counting using ADF STEM has been shown to be highly effective in facilitating the characterization of the three-dimensional atomic structure. Highly detailed ADF STEM images at the atomic level exhibit remarkable sensitivity to atom counts, enabling the precise quantification of atoms within every individual atomic column.[54,55]

The scattering cross-sections, ascertained by evaluating the collective electron scattering intensity for each atomic column, have proven to be a highly effective means for quantifying the atom count within a specific atomic column using a single STEM image.[54,56,57]

Utilizing the StatSTEM approach, one can construct a parametric model that characterizes the experimental images by superimposing Gaussian peaks positioned at the locations of atomic columns. The parameters of this model, which encompass the positions of the atomic columns, can subsequently be deduced through the least-

squares estimator[58].This empirical imaging model comprises a sum of Gaussian peaks from the intensities of atomic columns described as[59]:

$$f_{mix}(v_n;\ \psi_G) = \sum_{g=1}^{G} \pi_g \frac{1}{\sqrt{2\pi\sigma}} exp\ (\frac{-(V_n - \mu g)^2}{2\sigma^2})$$

This equiation it is called Gaussian mixture model and defines the probability of an specific scattering cross-section value Vn that would be stimated for a particular atomic column n. The vector describes as Ψ_G contains parameters that are unknown as π_g and μ_g that are the mixing proportion of the cross-section and the width of the peaks associated with a specific column type, which defines their "peakedness," is regarded as one of the unidentified parameters[56]. This unknown parameters has to be inferred from the scattering of the cross-sections.[59] The method consists in acquiring scattering cross-sections, individually for each atomic column, and subsequently translating these values into atomic counts. The overarching objective is to achieve atom-counting outcomes with exceptional precision and unwavering accuracy, as both are vital prerequisites for asserting single-atom sensitivity. In **Figure 8**, we observe the main interface of the statSTEM program with a TiO_2 particle.

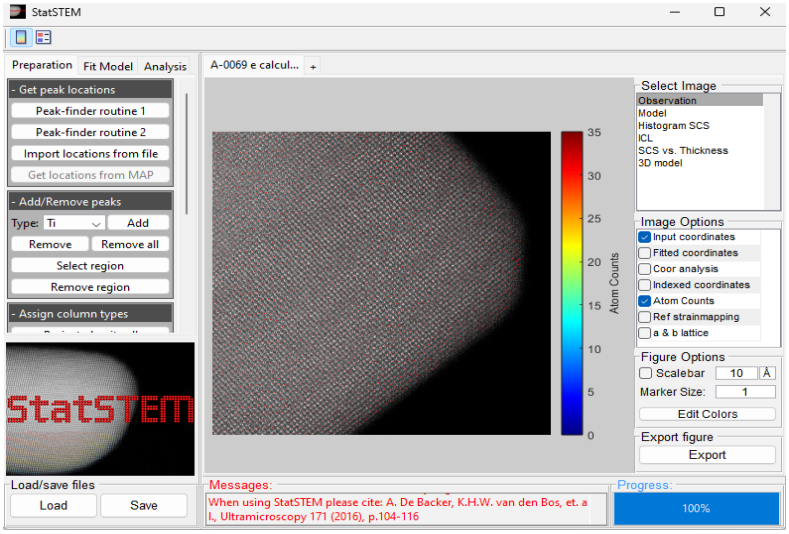

Figure 8. StatSTEM screen and functions

In Figure 8, the StatSTEM program screen is observed, where we can carry out atomic counting based on their approximation from the intensities obtained from direct atomic-resolution STEM micrograph images. The parameters of the crystal lattice being analyzed are entered, and the program locates the atomic positions. In addition to its capability to analyze the atomic column positions, it is possible to perform a 3D analysis that enables the observation of material facets.

6.5 IR / DRIFT

Diffuse Reflectance Infrared Fourier Transform Spectroscopy (DRIFTS) is a powerful analytical technique used in catalysis research for the characterization of catalysts and the investigation of surface species and adsorbed molecules. It utilizes infrared radiation to probe the vibrational modes of molecules on the catalyst surface. By measuring the changes in infrared absorption and reflection, DRIFTS provides valuable information about the surface chemistry, adsorption properties, and catalytic reactions occurring on the catalyst surface. This technique offers insights into the nature of active sites, the interaction between the catalyst and reactants, and the mechanism of catalytic reactions. It is a versatile tool for understanding the structure-function relationships of catalysts and designing more efficient catalytic systems. See in **Figure 9** the IR adapted with a DRIFT cell.

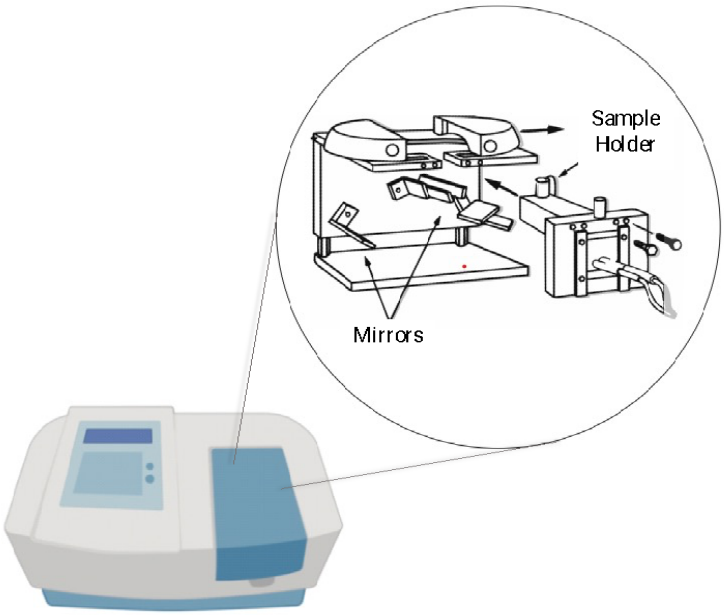

Figure 9. IR spectrometer adapted with a DRIFT cell.

DRIFTS works by irradiating the catalyst sample with infrared radiation and analyzing the resulting diffusely reflected light see **Figure 10**. The infrared radiation consists of a range of wavelengths that corresponds to the vibrational frequencies of chemical bonds in molecules. When the infrared light interacts with the catalyst surface, it is absorbed by the molecules present, causing them to vibrate and undergo changes in their dipole moment. These changes in dipole moment result in the scattering and reflection of the infrared light. Infrared spectroscopy is grounded in the inherent ability of any substance to absorb infrared radiation. This absorption phenomenon is intricately linked to the diverse vibrational modes exhibited by the molecules within a given sample, with particular relevance to catalytic processes or molecules adhered to a solid substrate. Each individual substance boasts a distinctive infrared absorption spectrum, serving as its unique signature. A fundamental criterion governing the absorption of photons lies in the requirement for a change in the molecule's dipole moment. The number of fundamental vibrations inherent to a

molecule hinge on the count of atoms denoted as "N" and whether the molecule assumes a linear or nonlinear configuration. For nonlinear molecules, the tally of fundamental vibrations is expressed as 3N-6, while for linear molecules, it stands at 3N-5.[47,60]

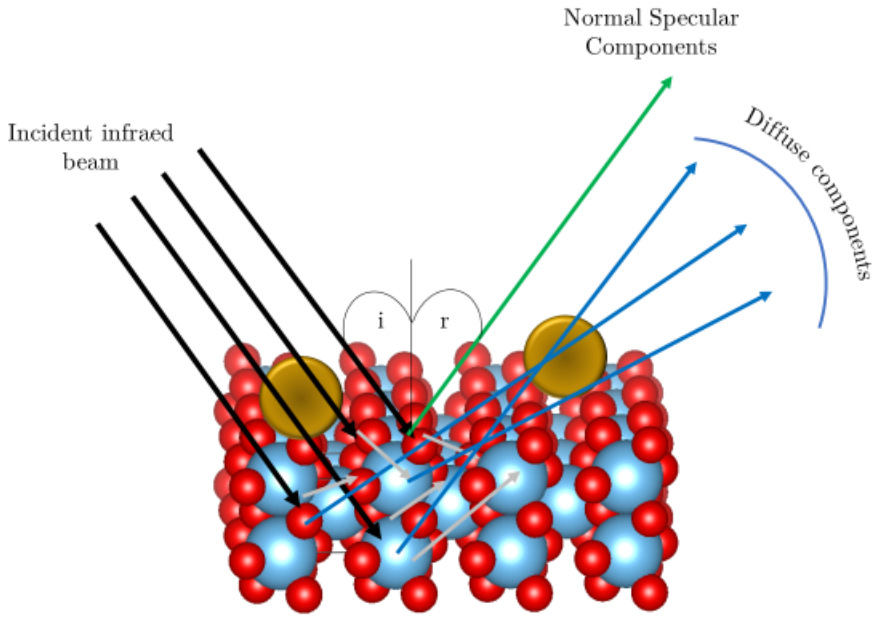

Figure 10. Diffuse Reflectance on material surface

The diffusely reflected light is collected by a detector, such as a Fourier Transform Infrared (FT-IR) spectrometer, which measures the intensity of the reflected light as a function of wavelength. This spectrum provides information about the vibrational modes of the molecules on the catalyst surface, allowing for the identification of specific functional groups and the determination of surface species[60].

By comparing the DRIFTS spectra of the catalyst before and after exposure to reactants or under different reaction conditions, researchers can gain insights into the adsorption and desorption processes, the formation of reaction intermediates, and the overall catalytic activity.

In the realm of single-atom catalysts (SACs), DRIFTS assumes a prominent position as an infrared spectroscopy technique widely embraced in the field of catalysis. Its primary utility lies in the identification of adsorbed species and the monitoring of their transformations as chemical reactions progress. Consequently, DRIFTS offers valuable insights into the stability, uniformity, and oxidation state of the active species under investigation. Within the context of DRIFTS studies, carbon monoxide (CO) frequently serves as a probe molecule, facilitating the observation and analysis of the dispersion and oxidation state of noble metal sites exposed on supported catalysts. [61,62]

6.6 X-ray Photoelectron Spectroscopy

X-ray photoelectron spectroscopy (XPS) is a highly valuable analytical method employed in catalysis research for the examination of catalyst surfaces. Its primary purpose is to investigate the surface composition and chemical states of catalyst materials. By utilizing X-ray photons to induce the emission of inner-shell electrons from atoms within the catalyst, XPS allows for the measurement of electron kinetic energy and intensity. This data yields crucial information regarding the elemental composition, oxidation states, and bonding environments present on the catalyst surface.

Within the realm of catalysis, XPS plays a central role in elucidating surface chemistry and catalytic reactivity. It facilitates the exploration of active sites and their electronic structures, which are fundamental to catalytic processes. Through XPS, researchers can explore alterations in the oxidation states of catalytic metals under reaction conditions, observe adsorbed species or reaction intermediates, and

analyze the impact of environmental factors like temperature and pressure on the catalyst surface[63].

Furthermore, XPS proves to be an invaluable tool for both pre- and post-reaction analysis of catalysts. It enables the detection of surface modifications, the clarification of catalyst deactivation mechanisms, and the determination of catalyst stability. The technique is also suitable for in situ characterization, enabling real-time monitoring of catalyst performance during catalytic reactions.

n X-ray photoelectron spectroscopy (XPS), a focused X-ray beam, often containing k-alpha X-rays, is targeted at the sample. See **Figure 11**. The absorption of these incident X-rays leads to the emission of electrons. The detector is then employed to measure the energy of these emitted electrons, furnishing essential information regarding the sample's composition and chemical states[64].

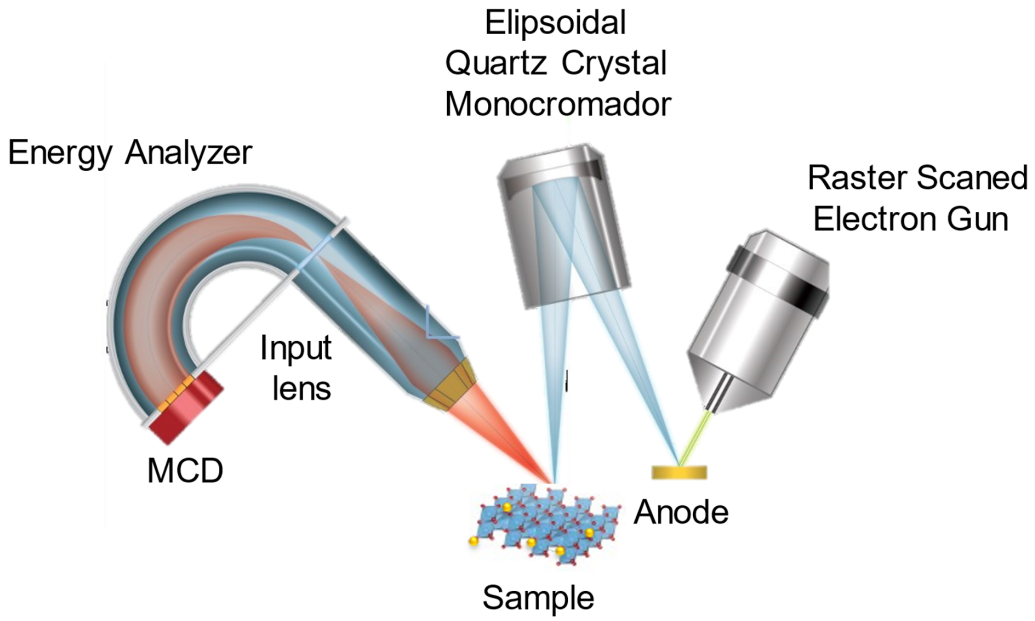

Figure 11. XPS system

XPS relies on the photoelectric effect, which is the process where a material exposed to a photon flux with adequate energy results in the emission of electrons, known as photoemission. The technique involves measuring the kinetic energy (EK) of the

emitted electron and determining its binding energy (EB) for a specific energy level, as defined by the Einstein relationship Equation.[65]

$$E_k = hv - E_B$$

Here, the incident radiation's energy hv level comes into play. In XPS, the incident photon energy typically exceeds 1200 eV, which is sufficiently energetic to eject electrons from the core levels of atoms. EB does not precisely correspond to the electron's orbital energy due to what's known as the frozen-orbital approximation. EB is formulated as follows:

$$EB = Ei - Ef$$

Where Ei represents the total energy of the initial (ground) state, and Ef signifies the total energy of the final (ionized) state see **Figure 12**. When equations are integrated, it becomes evident that any factors influencing the initial or final state of the emitting atom will exert an impact on the binding energy.[65]

Analyzing the distribution of kinetic (binding) energies concerning the photoelectron flux provides the photoelectron spectrum, revealing all the available energy levels.

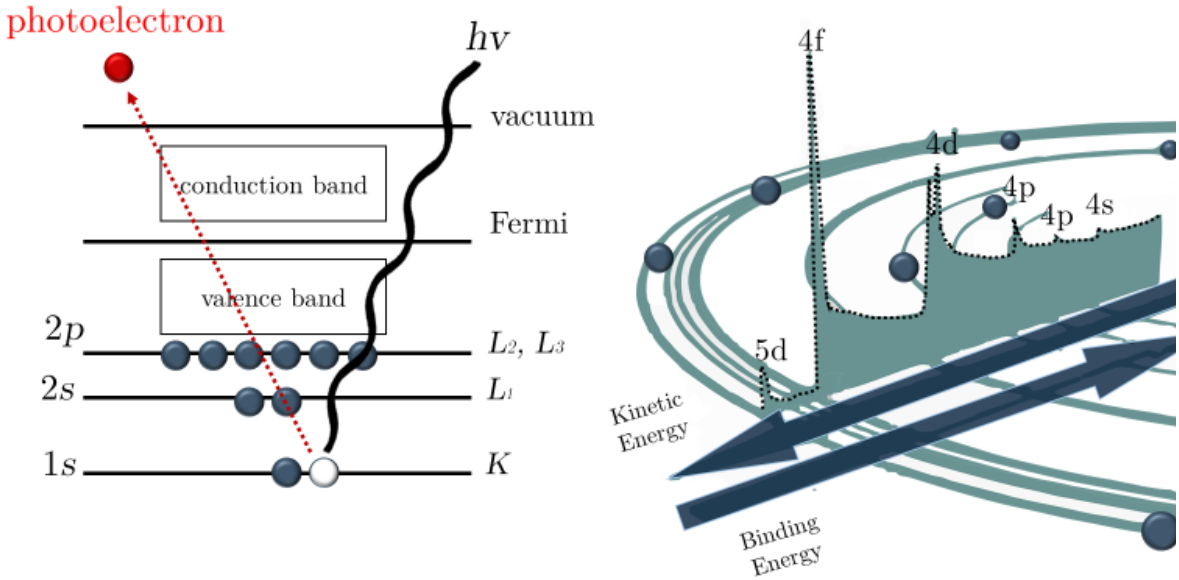

Figure 12. How XPS works

When an atom engages in chemical bonding with another atom, it results in a modification of the valence electron density, thereby leading to an adjustment in the electrostatic potential that influences the behavior of core electrons. As a consequence, variations in the binding energies of core electrons are responsible for inducing shifts in the corresponding photoelectron peaks. Specifically, when an atom experiences a reduction in valence charge, its binding energy exhibits an increase, whereas an increase in valence charge corresponds to a reduction in binding energy
In summary, X-ray photoelectron spectroscopy stands as an indispensable technique in catalysis research, offering valuable insights into the surface chemistry and reactivity of catalysts. Its capability to probe atomic-scale properties of catalyst surfaces provides essential information for comprehending catalytic mechanisms, optimizing catalyst design, and advancing the development of more efficient and selective catalytic processes. Additionally, XPS allows for the determination of the oxidation state of iridium, providing valuable insights into its chemical state.

6.7 CO Oxidation

CO Oxidation has been placed by a chromatograph of gas. Gas chromatography is an analytical method employed to isolate the chemical constituents within a sample mixture and subsequently identify them to establish their presence or absence. Moreover, it is utilized to quantify the amount of these constituents within the sample. Gas chromatography stands as an essential tool to recognize, and measure the constituent compounds within a mixture, in this case a catalyst.

The process involves a constant flow of carrier gas through a column containing a stationary phase. The process of chromatographic analysis commences with the

introduction of a test mixture into the inlet of the column. While traversing the column, different solutes within the mixture interact and migrate. Consequently, each solute becomes temporarily held within the column see **Figure 13**, known as its retention time. Varied retention times lead to the individual elution of solutes, causing them to exit the column outlet separately, thus achieving the separation of these components. When the eluted mixture, combined with the mobile phase, passes through the detector, it triggers a response indicating the presence and quantification of the solute.

This observation is typically represented through a plot showing the time elapsed since the injection of the test mixture[66].

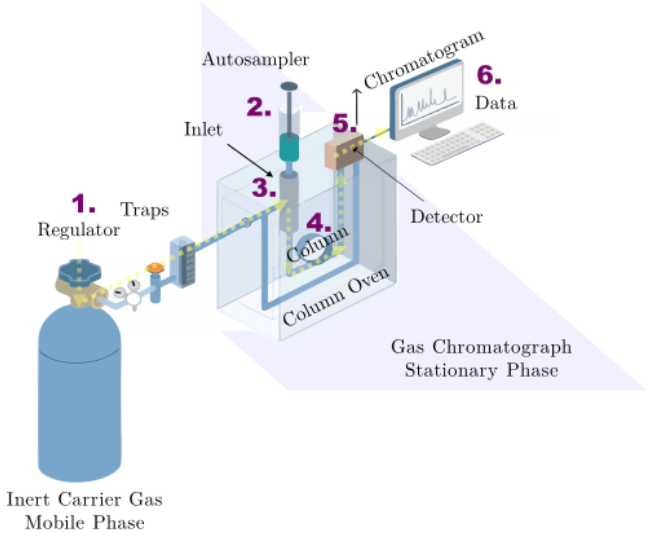

Figure 13. Temperature Programmed Gas Chromatography

Two fundamental techniques are classified based on the temperature distribution within the column. In temperature programming, a fixed temperature gradient traverses the column, resulting in varying temperatures along its length. The movement of the gradient furnace corresponds to the shifting position of solute bands along the gradient[67].

- Carrier Gas: The carrier gas acts as the conduit to transport the injected sample through the system. The chosen gas must be inert to both the sample and the column packing material. It is crucial to remove any residual moisture or other gaseous impurities.
- Injectors: Injectors are used to ensure a consistent volume injection of the sample into the carrier gas flow. Maintaining inertness and reproducibility during injection is essential to maintain a high level of accuracy. Injectors must be capable of handling small volumes in the microliter range with the utmost precision.
- Column: Gas chromatography employs columns that can be either short-length stainless steel or glass (approximately 1.5-2 meters) or long-length (30 meters or more). Capillary columns consist of flexible fused silica tubing, while packed columns are filled with a stationary phase. Capillary columns feature a layer of absorbing material on their inner walls. Proper maintenance, following supplier instructions, is essential for ensuring long-term usage and consistent separations run after run.
- Column Oven: The column oven serves as the housing for the column, maintaining either a constant temperature (isothermal operation) or variable temperature, depending on the analysis requirements (temperature programming).

Modern Gas Carrier systems are computer-based, with software controlling operational parameters such as carrier gas flow rate, temperature programming, injection volume and sequence, as well as data acquisition and analysis[68].

7. Methodology

Protocol for the synthesis of monodispersed samples

Reagents

TiO_2(IV) was used as the support material (Sigma-Aldrich 637262), in the rutile phase with particle size below 100nm. The powder was dried for two hours at 100°C prior to each synthesis. The iridium precursors used were iridium (III) $IrCl_3xH_2O$ and [Ir(acac)3] $C_{15}H_{21}IrO_6$. Urea (ACS Reagent, Sigma Aldrich) was used as the precipitating agent.

7.1 Deposition precipitation with urea

Incorporation of the active phase

The incorporation of iridium was done using the deposition-precipitation with urea (DPU) method [32,69,70]. A nominal amount of iridium $IrCl_3$ at 0.25% by weight was used relative to the support. **Figure 14** graphically summarizes the synthesis method, where initially, 0.5 g of pre-dried support, as well as Ir salt and urea, were weighed. Urea and $IrCl_3$ were dissolved separately in water before the reaction, and then added to the reactor. We started with the dry titanium oxide, then added the $IrCl_3$ solution, and subsequently the urea solution once it reached a temperature of 80 °C. We waited for 5 hours, monitoring the pH change. Once the reaction time was completed, we proceeded to wash the samples to remove chlorides from the precursor. We performed 4 washes with deionized water at 12,000 rpm for 10 minutes each. Subsequently, the sample was dried at 100 °C for later storage and hydrogen reduction.

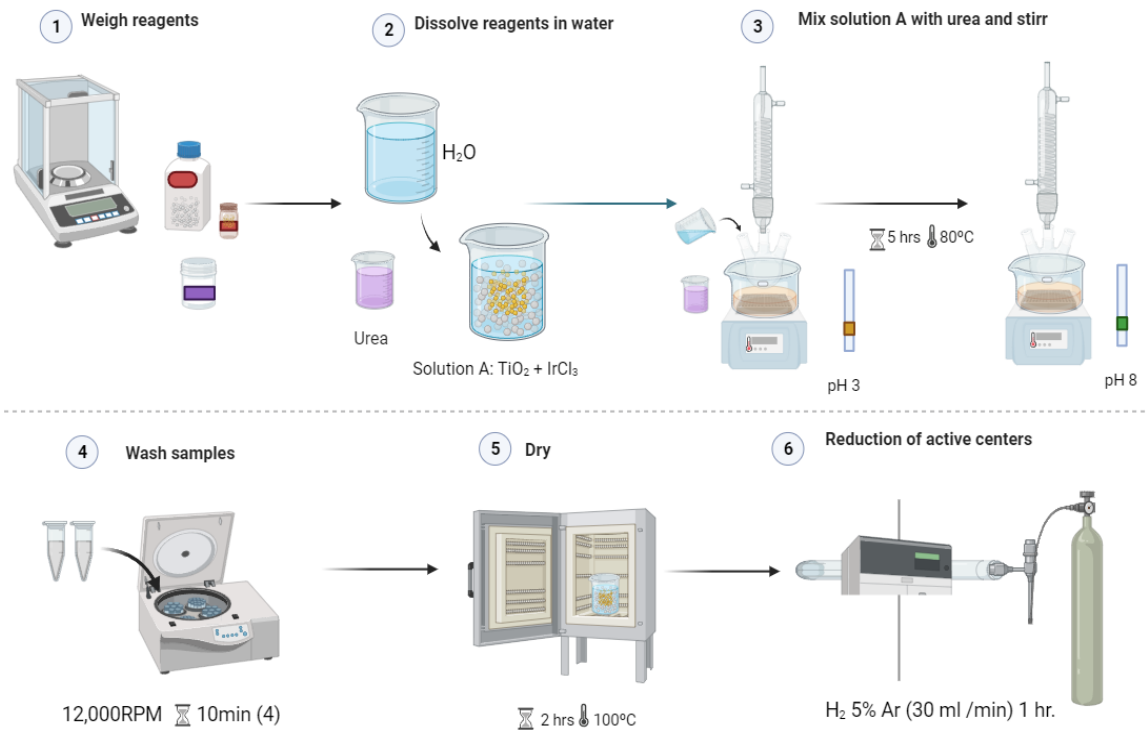

Figure 14. Deposition-precipitation method with urea and sample reduction.

7.2 Impregnation

A stock solution of Ir was prepared using the precursor $C_{15}H_{21}IrO_6$. The solution's content was calculated to contain 0.25 %wt of Ir in 25 mL of chloroform.

Wet impregnation technique was employed for the incorporation of iridium in solution[32]. The catalyst was prepared by the incipient wetness method with a nominal loading of 0.25% by weight of [Ir(acac)3] $C_{15}H_{21}IrO_6$ respect to the support. **Figure 15** summarizes the synthesis method where the impregnation solution was added drop by drop to the support under magnetic stirring. Subsequently, the system was maintained at a temperature of 60 °C until the solvent was evaporated. The material was then dried at 100 °C for 3 hours.

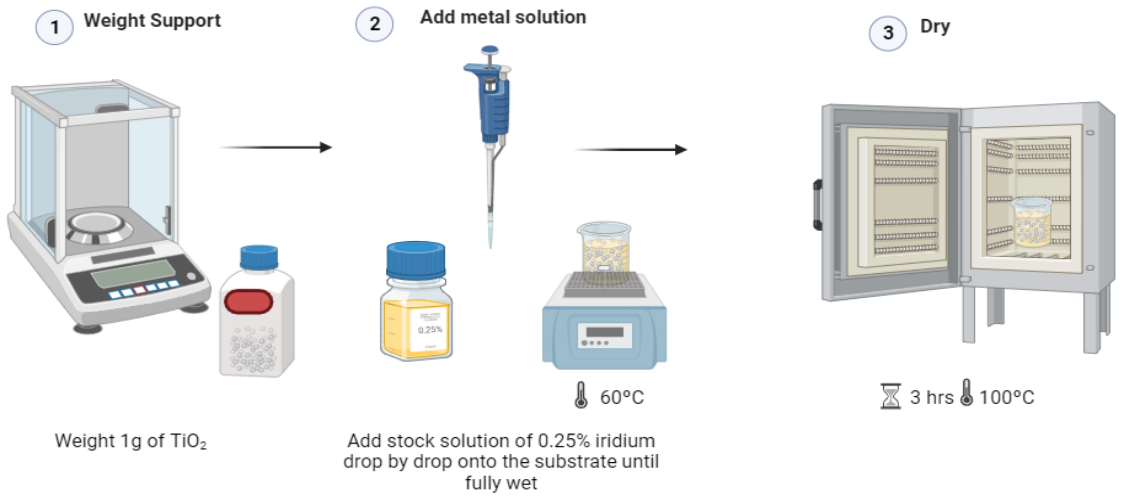

Figure 15. Impregnation method for Ir/TiO_2 SAC

Several parameters were varied and monitored during the synthesis, including reaction time, pH changes, the nominal amount of iridium on the support, and, most importantly, morphological changes when carrying out calcination and reduction treatments at 300 and 400°C, in order to determine the optimal conditions for synthesizing Ir-SACs. **Table 3** displays the conducted syntheses, the labels of the samples, preparation method, synthesis, and thermal treatments conducted.

Table 3. Proof synthesis of catalyst based in Ir/TiO_2

Sample	**Synthesis**	**Precursor**	**Metallic %wt**	**Time reaction (hrs.)**	**pH change**	**Calcination** (°C)	**Activation** (°C)
A	DPU	$IrCl_3$	0.25	5	3 to 6	300	...
B	DPU	$IrCl_3$	0.25	17	4 to 8	...	400
C	DPU	$IrCl_3$	0.25	16	4 to 8	...	300, 400
D	DPU	$C_{15}H_{21}IrO_6$	0.25	17	4 to 8	...	400
E	DPU	$C_{15}H_{21}IrO_6$	0.15	17	4 to 8	...	400
F	DPU	$C_{15}H_{21}IrO_6$	0.5	17	4 to 8	...	400

G	DPU	$IrCl_3$	0.15	17	4 to 8	…	300, 400
H	DPU	$IrCl_3$	0.5	18	4 to 8	…	400
K	Impregnation	$C_{15}H_{21}IrO_6$	0.25	…	…	300	…
L	Impregnation	$C_{15}H_{21}IrO_6$	0.125	…	…	300	…
M	Impregnation	$C_{15}H_{21}IrO_6$	0.25	…	…	300	300
N	Impregnation	$C_{15}H_{21}IrO_6$	0.5	…	…	300	…

Synthesis **A, B** and **M** were chosen as objects of study due to their high iridium dispersion. This characteristic makes them particularly interesting for the detailed analysis aimed to be carried out in this research project. In order to ensure the reliability and consistency of the results, it was decided to repeat these two syntheses on multiple occasions. This approach was selected with the purpose of verifying the reproducibility of the procedures used and ensuring that the results are not the product of random variations or experimental errors; thus, allowing us to establish a solid foundation of data and observations to support the conclusions of this study.

8. Characterization

8.1 X-ray Diffraction

X-ray diffraction (XRD) technique was used to analyze the crystal structure, phases present, and composition of the components of the material under study. XRD is a powerful tool as it provides a wide range of information about crystallographic parameters, including symmetry, material structure, lattice configuration, and interatomic distances.

The D8 ADVANCED equipment was used, which has the capability to measure various types of samples, from liquids to thin films. It features a Cu anode (λ= 1.54 Å) that can move at a rate of 2° per minute. The sample was directly mounted on a silica oxide sample holder.

8.2 Transmission Electron Microscopy

In the context of this thesis, materials were characterized using transmission electron microscopy (TEM) technique. High-resolution transmission electron microscopy (HRTEM) and high-resolution scanning transmission electron microscopy with high-angle annular dark-field imaging (HAADF-STEM) are highlighted as fundamental techniques for evaluating heterogeneous catalysts composed of small-sized metal particles supported on high surface area substrates. The catalytic activity of these materials is directly related to the number of atoms present on the support surface, as well as the structure and spatial distribution of the metal particles, thus making it convenient to minimize their size.

In this research, a Jeol ARM-200F microscope located at the Laboratorio Universitario de Microscopía Electrónica (LUME@UNAM) was used, which allows obtaining images in scanning transmission mode (STEM). The acceleration voltage was set to 200 keV, taking advantage of the presence of a CESCOR spherical aberration corrector, allowing for a resolution of 0.78 Å. Specifically, the Cs-HAADF-STEM technique was employed, which provides detailed information about the composition and distribution of elements in the analyzed sample. The convergence and collection semi-angles were set to 25 mrad and 68-220 mrad, respectively. The chemical composition of the studied materials was confirmed by EDS, using an energy dispersive X-ray spectrometer Oxford AztecTEM coupled to the TEM.

For observation in the microscope, sample preparation was carried out by dispersing the solid in isopropanol using ultrasonication. Subsequently, a small amount of the dispersion was extracted and deposited on a gold grid coated with amorphous carbon.

The processing of TEM and HRTEM images was performed using Gatan Digital Micrograph software. To obtain high-resolution atomic-level images and study the material's crystallographic orientations, the Fast Fourier Transform (FFT) technique was used. SimulaTEM was used to obtain simulations based on HAADF-STEM micrographs of TiO_2 support with a Ir in a Ti column.

8.3 Analysis of Temperature Programmed Reduction

The technique known as Temperature Programmed Reduction (TPR) is employed as a highly effective method for the chemical characterization of various materials, providing precise information about their reduction properties. This technique is based on generating controlled temperature profiles, which allows a detailed analysis of material behavior in response to specific thermal changes during reduction processes.

Thermal treatments were conducted in a high-temperature GSL-1100 vacuum tube furnace. Two different thermal treatments were proposed to analyze the effect of temperature on the Ir/TiO_2 systems see **Table 4**. The following reduction tests were performed, both under a reducing atmosphere of 5% H_2/Ar for one hour.

Table 4. Temperature ramps in reduction tests.

System	**Temperature ramp**
$Ir/TiO_{2\text{-DPU}}$	TR(1): 10° C x 10 min from environment temperature to 100° C, TR(2): from 100° C to 300° C
$Ir/TiO_{2\text{-DPU}}$	TR(1): 10° C x 10 min from environment temperature to 100° C, TR(2): de 100° C a 400° C

The study samples were subjected to a temperature-programmed reduction process using an RIG-100 equipment. This equipment is equipped with a quartz reactor of 8 mm internal diameter and a fixed bed of ceramic material. Additionally, it has a TCD detector to monitor the H_2 consumption and valves that allow measuring gas flow. Moreover, it has a temperature-controlled furnace capable of reaching up to 1000°C.

A prior calcination treatment was carried out before the reduction, up to 300°C in air, using a heating ramp of 10°C/min and an N_2 cooling purge. The equipment is equipped with a silica container containing a humidity indicator, designed to trap water generated during the reduction process to avoid possible interferences with the TCD detector.

A 5% H_2 in N_2 gas mixture (30 ml/min) was supplied during the temperature increment with the aim of generating intensity curves in relation to the temperature, in terms of H_2 consumption during the process. Temperature-programmed reduction was implemented for samples A, M, and TiO_2 support using approximately 0.050 g of each sample. Finally, the reduction of the samples was carried out through a thermal treatment in H_2, using a heating ramp of 2°C/min from room temperature to 300°C for one hour.

Table 5. Thermal treatments for catalysts.

System	Sample	Treatment
Ir/TiO_2	A	H_2, 300°C
Ir/TiO_2	M	H_2, 300°C

8.4 CO Adsorption followed by Diffuse Reflectance

Infrared spectroscopy in the Diffuse Reflectance (DRIFT) mode was conducted, a useful characterization technique to study the nature of species on the surface of a catalyst. This technique is based on measuring the infrared radiation diffusely reflected from the sample, aiming to obtain information about the material's composition and molecular structure. In CO adsorption, carbon monoxide is used as a probing molecule that serves as a reference in its interaction with the support, providing information about the oxidation state of active phases.

In this research, a Nicolet iS50 FTIR spectrometer was used, equipped with an MCTA detector, a resolution of 4 cm^{-1}, and 128 scans, with a PIKE Diffuse IR cell featuring controlled atmospheres, temperature control, and a KBr window.

Prior to the DRIFT analysis, an in-situ pre-treatment is performed with 10% H_2/N_2 at a flow rate of (30 ml/min) at 300°C for one hour. Then, a purge with N_2 (30 ml/min) is carried out. Subsequently, the temperature is cooled down to 200°C, 150°C, 100°C, 50°C, and 25°C.

The CO adsorption experiment is conducted at 25°C using a gas mixture of 1% CO/Ar (30 ml/min) for one minute. Afterward, a purge with N_2 (30 ml/min) is performed, and spectra are taken at 25°C, 50°C, 100°C, 150°C, and 200°C to observe the desorption of the gas.

8.5 X-ray photoelectron spectroscopy

The surface composition analysis of the samples was assessed through X-ray photoelectron spectroscopy (XPS). A Physical Electronics system equipped with a scanning XPS microprobe (PHI 5000 VersaProbe II) was utilized, using the Al Kα (hν = 1486.6 eV) signal. The survey spectra were recorded with a pass energy of 117.4 eV, and high-resolution spectra at 23.5 eV were obtained.

To ensure the accuracy of the analysis, only a very small amount of samples A, M, and the support were used as references during the measurements. Additionally, Ar cleaning was intentionally avoided during the process to prevent any modifications in the oxidation states of both Mn and Co. To correct the binding energies, the spurious C1s signal at 284.8 eV was employed. The data analysis was performed using Multipack© software version 9.6.0.15.

8.6 Inductively Coupled Plasma Mass Spectrometry

The study was conducted using an Inductively Coupled Plasma Mass Spectrometer, THERMO SCIENTIFIC ICAP Qc, ICP-MS, and an X-ray Fluorescence Spectrometer, RIGAKU NEXQC+.

The systems were digested in a HCl/HNO3 solution (1/3 v/v) at 75°C under reflux for 14 hours. Subsequently, they were diluted to 100 ml and adjusted with distilled water. Then, they were allowed to rest for 3 weeks for complete metal dilution.

9. Catalytic Reactivity

9.1 Oxidation of CO

The $CO+O_2$ reaction was studied using an Agilent Technologies 7820 A gas chromatograph equipped with an Agilent CP-Sil 5 CB column (0.32 mm x 50 m). The instrument is fitted with a Flame Ionization Detector (FID) and a methanizer, enabling the conversion of organic compounds to methane for more efficient detection. For the analysis, 40 mg of the catalyst was used. The samples analyzed were A and M to compare the adsorption of CO which were synthesized differently. The reaction was initiated from room temperature and raised to 300°C at a heating rate of 2 °C/min, staying at that temperature for one hour in flowing hydrogen before measuring the catalytic activity. Thereafter, the catalysts were cooled to room temperature under the same atmosphere.

During the reaction, the feed gas contained 1% CO, 1% O_2, and 98% N_2, and it was passed over the catalyst at a flow rate of 100 mL/mins.

10. Results and Discussion

In this chapter, the results of the characterization of TiO_2-Support, Ir/TiO_2-DPU, and Ir/TiO_2 -Impregnation systems are presented.

10.1 X-ray Diffraction

Figure 16 shows the X-ray diffractogram of the TiO_2 support, the Ir/TiO_2 -DPU, and the Ir/TiO_2 Impregnation systems. The comparison of the diffraction angles corresponds to those associated with the PDF 01-078-4190 card, whose phase is rutile. The intensity of the peaks indicates high crystallinity, with a tetragonal phase having lattice parameters a=b=4.5933 Å, c=2.9592 Å. This information played a crucial role in the examination and analysis of the micrographs, as well as in their simulation using StatSTEM.

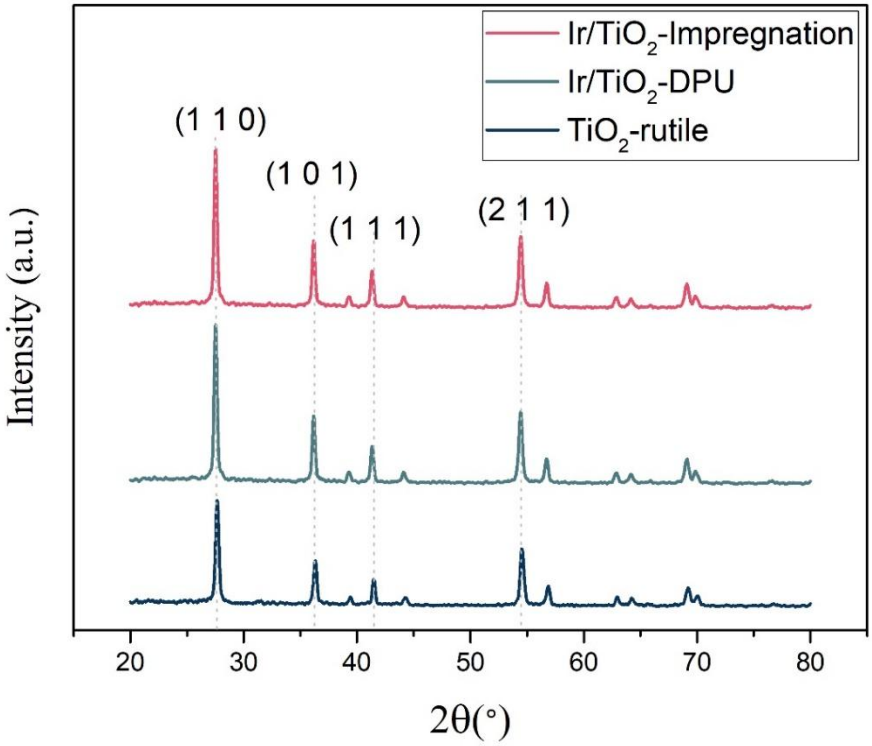

Figure 16. DRX to TiO_2, Ir/TiO_2 -DPU and Ir/TiO_2 Impregnation systems. TiO_2 corresponds to the rutile phase and there are no peaks related to iridium observed.

As observed in the rutile crystalline structure, the results suggested that iridium atoms were highly dispersed on the support, as there is no difference in the X-ray diffraction spectra between TiO_2 and Ir/TiO_2 -DPU and Ir/TiO_2 Impregnation systems. Additionally, the distinctive peaks associated with metallic Ir species (2θ = 40.6° (111) and 47.3° (200) were not detected[71]. It can be noted that it is not incorporated into the support, neither as nanoparticles, as there are no changes in the diffraction peaks, and only the peaks corresponding to rutile were observed.

10.2 Scanning Transmission Electron Microscopy and Stat-STEM

The synthesized samples were analyzed by HAADF. In **Figure 17**, samples A to H were synthesized using DPU, while samples K to N were synthesized through impregnation. **Figure 17** depicts the HAADF images of various Ir/TiO_2 systems. **In Figure 16a**, sample **A** corresponds to the synthesis **A** of **Table 3**. The synthesis method was followed by HAADF-STEM, demonstrating a high dispersion of iridium atoms. However, the established reaction time by Zanella et al. had not been completed; therefore, we proceeded with the method as prescribed. The TiO_2 morphologies remain unaltered after loading, showcasing the remarkable stability of the TiO_2 supports.

In the HAADF-STEM images in **Figure 17b-d**, it is evident that iridium nanoparticles (NPs) have formed, clearly observed with an approximate radius of 2 nm. This outcome may be attributed to the synthesis method and the temperature treatments. In **Figure 17e-f**, we observe that with a lower nominal metal loading, small clusters and dispersed atoms are visible. These clusters might be related to the temperature treatments. In **Figure 17g-h**, we varied the supported metal content, resulting in the observation of small iridium clusters.

The corresponding HAADF-STEM images of the Ir/TiO_2 systems in Figure **17k-n** reveal iridium as single atoms dispersed on the surface of TiO_2. Varying the nominal metal content does not show significant differences in the image samples. It is shown that the impregnation method has proven to be an effective approach for creating facile single iridium catalysts.

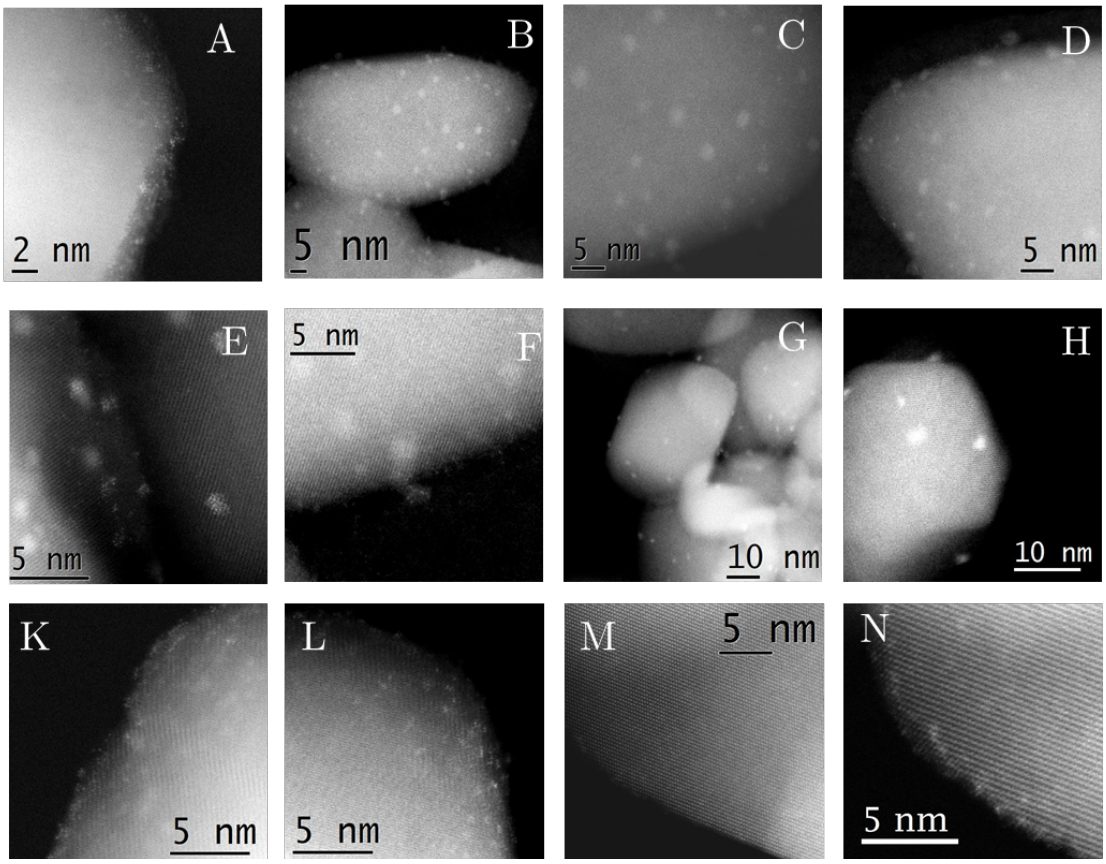

Figure 17. Various Ir/TiO_2 systems. HAADF-STEM images of synthesis performed in this work, refer to Table 3 sintetized by DPU from A-K and impregnation from L to M.

The **A** and **M** syntheses were successfully repeated to verify their reproducibility. From now on, the results will be presented for these two samples only. Synthesis A was labeled as "**Ir/TiO_2-DPU**," and Synthesis M was designated as "**Ir/TiO_2-Impregnation**.

TiO_2 Crystals

To estimate the crystal shape and exposed facets of TiO2, HRTEM images were acquired.

The image processing was conducted using Digital Micrograph. HR-TEM images for obtaining zone axes were acquired through Fourier transforms. From there, the angles of the crystal facets were determined, assisting in identifying the faces more likely to be present in TiO_2. In this case, it was more common to find TiO2 crystals in the [001] and [111] zone axes. As depicted in **Figure 18**, the larger facet is [110].

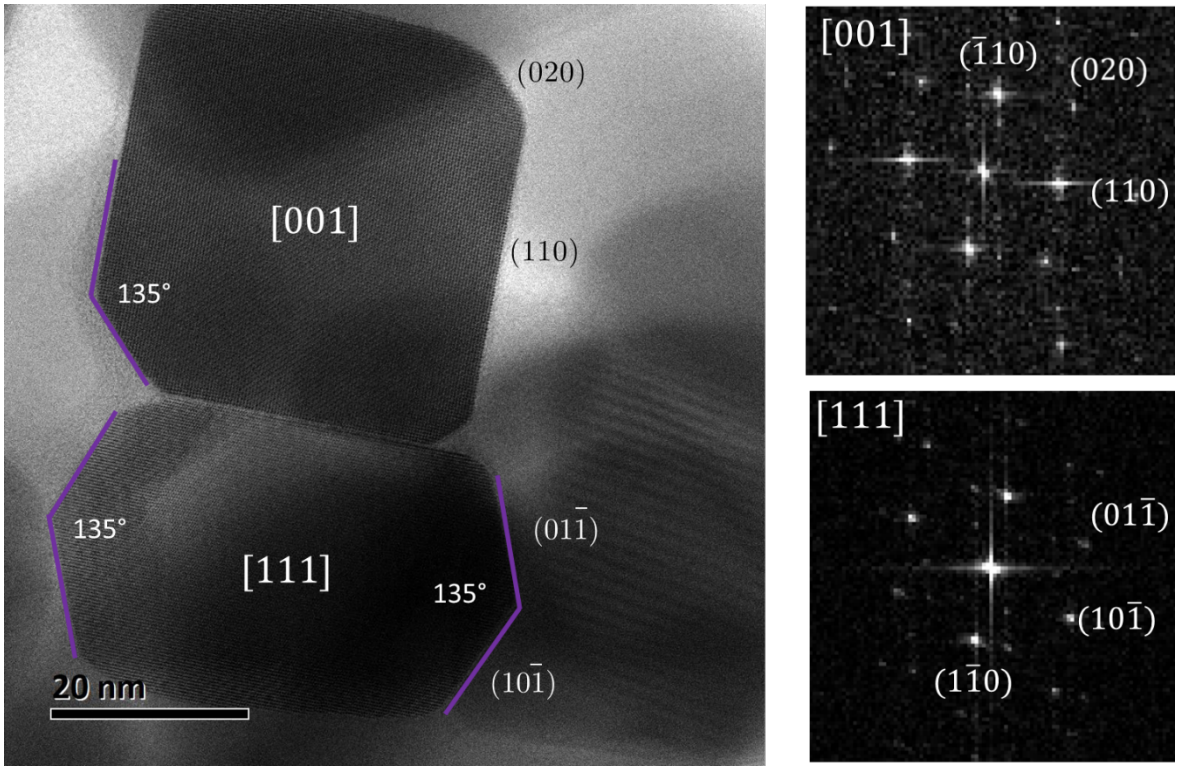

Figure 18. Zone axis of facets in TiO_2 and diffraction pattern and FFT patterns

HR-TEM was performed to analyze the crystal morphology of the support TiO_2. The crystal was recreated by obtaining the angles and crystal parameters. The crystal was constructed based on references [72,73]. In **Figure 19,** the HR-TEM micrograph of a TiO_2 rutile phase crystal is presented. The crystal facets were

colored in red for the [100], green for [100], blue for [111], and dark red for [001].

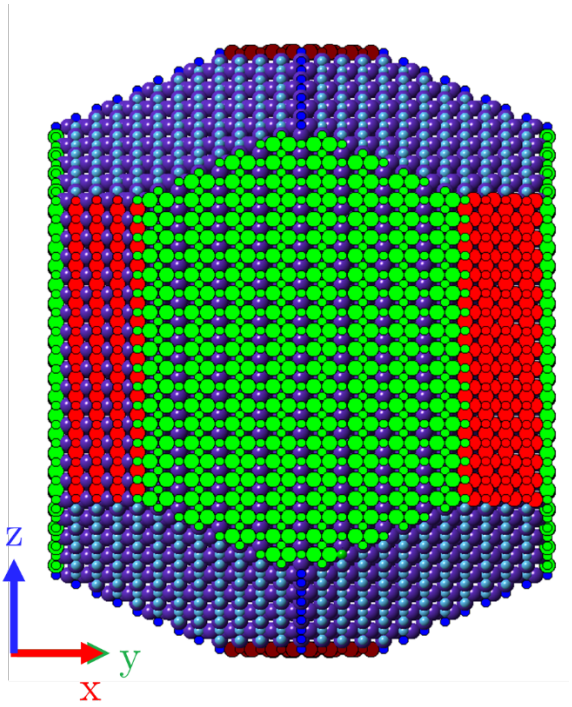

Figure 19. Facets of TiO_2 where the facets in green are the ones that correspond to (110), the red ones to (100), the little wine one to (001) and the purple ones to (101).

With the information obtained from the TEM micrographs and the clearer image with the modeled crystal, STEM of the support was performed. By achieving atomic resolution in the micrographs, it is possible to recreate the crystal in StatSTEM. The tip of a TiO_2 crystal was modeled, and facets are observed, as proposed by the model. In **Figure 20a** the micrograph for analysis and **Figure 20b, 20c** StatSTEM 3D

model. In this figure the red columns are Ti and the green ones O. The TiO_2 crystal thickness diminishes from the center to the edge, as evident from the observation.

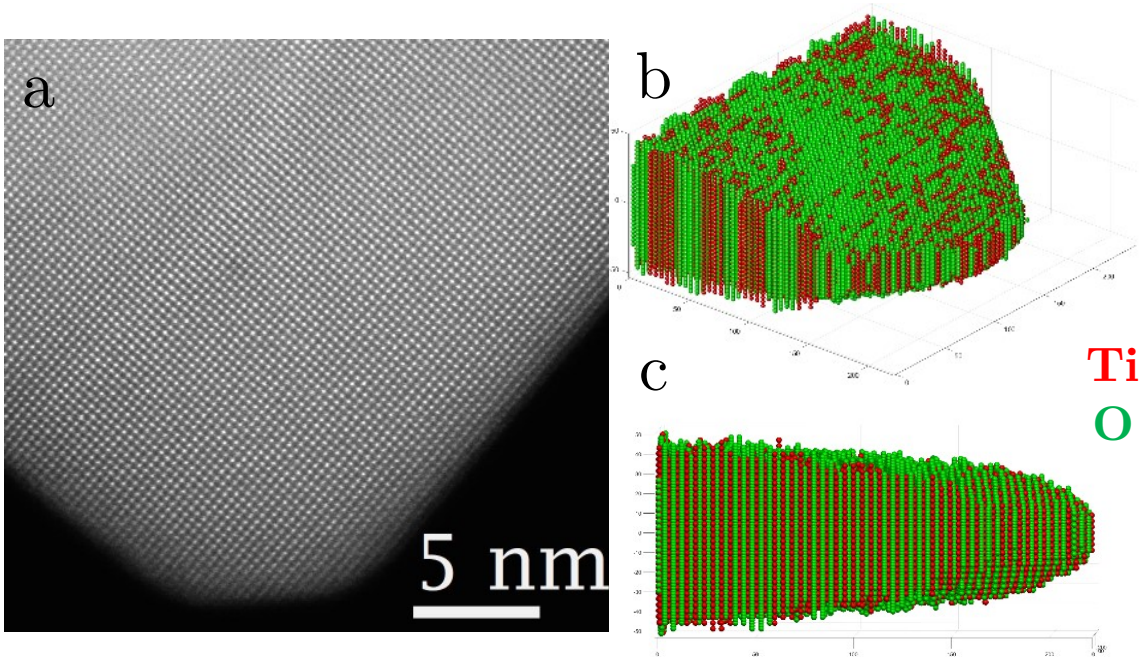

Figure 20. HAADF-STEM to TiO_2 support and StatSTEM 3D model. In (a), a corner of the crystal was examined using HAADF-STEM. This image was later rendered in 3D using StatSTEM and randomly projected in (b) and (c) to allow for navigation within the crystal.

The acquisition of high-resolution TEM micrographs allowed for the precise examination of the crystal's orientation, revealing the prominent presence of the [111] and [001] zone axes as is shown in **Figure 21 a-b**. These orientations were distinctly evident in the reconstructed crystal lattice.

The [111] zone axis appeared as a prominent, well-defined pattern, highlighting the crystal's alignment in this direction. Similarly, the [001] zone axis exhibited clear and distinct characteristics, providing valuable insights into the crystal's atomic arrangement along this axis. The analysis of these zone axes contributed significantly to our understanding of the crystal's structural features and provided essential information for locate iridium atoms.

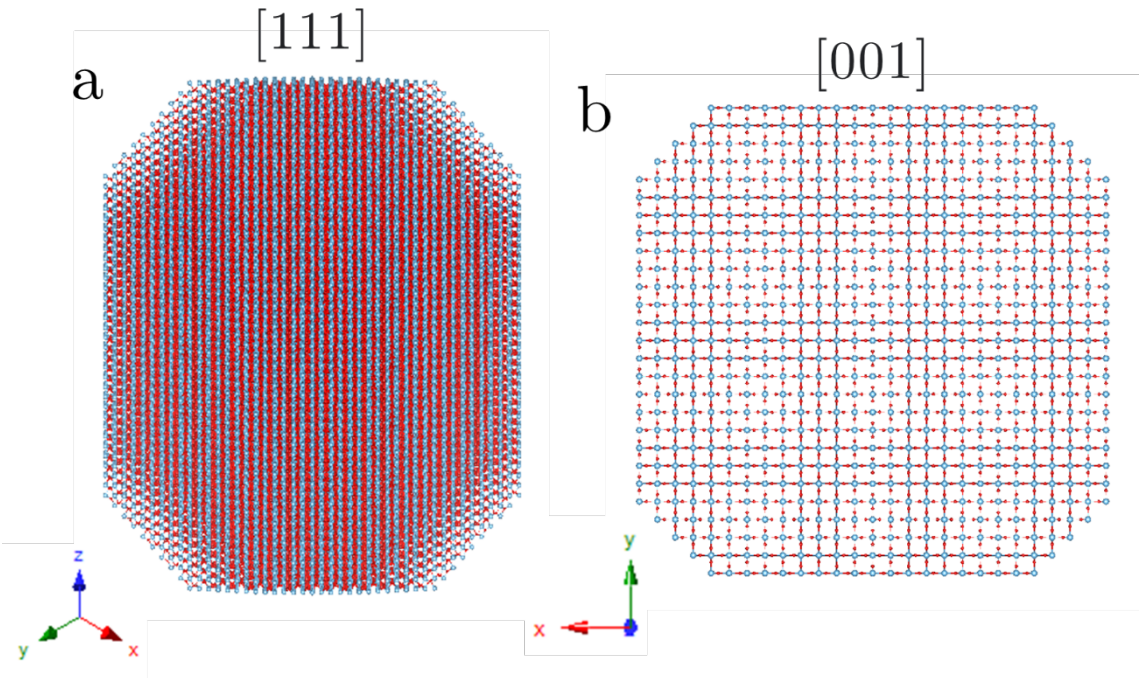

Figure 21. Orientations of TiO_2 crystal lattice projected in the [111] and [001] zone axes.

Ir/TiO_2-DPU

Using HAADF-STEM, the result of the synthesis was observed. It was noted that when well-oriented TiO_2 crystals were encountered, it was extremely challenging to distinguish between iridium (Ir) and titanium (Ti) atoms, despite their differences in atomic number Ir Z=79 Ti Z=22 see **Figure 22**.

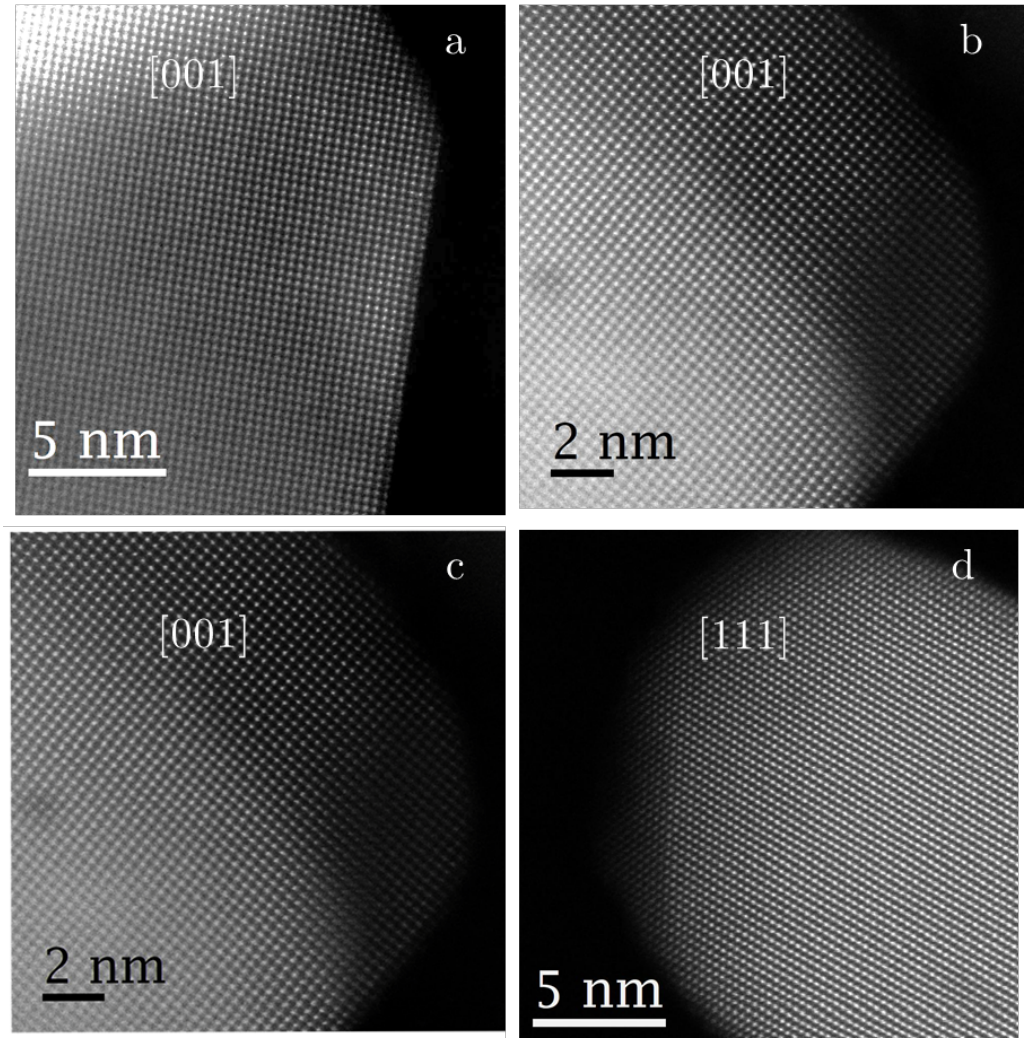

Figure 22. HAADF-STEM images of Ir/TiO_2-DPU

In the thinner regions of the crystal, the presence of some more intense atoms is observed, which are attributed to the presence of iridium. It is also evident that the crystalline order of TiO_2 is preserved, meaning that the iridium atoms occupy titanium positions on the crystal's surface.

Observations in the thinner sections of the crystal reveal the heightened intensity of certain atoms, indicative of the presence of iridium. Additionally, the crystalline structure of TiO_2 remains intact, signifying that iridium atoms have assumed titanium positions on the crystal's surface.

As seen in **Figure 23a** HAADF-STEM image of Ir/TiO_2 **in Figure 23b** intensity profiles were generated using Image J to highlight the presence of iridium atoms; however, the distinction was not as evident as anticipated. This led to further investigation using TEM image analysis software, such as StemCell.

Utilizing the information acquired from the StatSTEM model, a TiO_2 crystal serves as the support, and the simulated cell contains 34 titanium atoms. **In Figure 23c**, the column of Ti modified with iridium atoms on the surface is highlighted in yellow in **Figure 23d**. In **Figure 23c**, it can be observed that for one iridium atom, nevertheless, the intensity profile analysis was selected within the purple rectangle, as seen in **Figure 23d**.

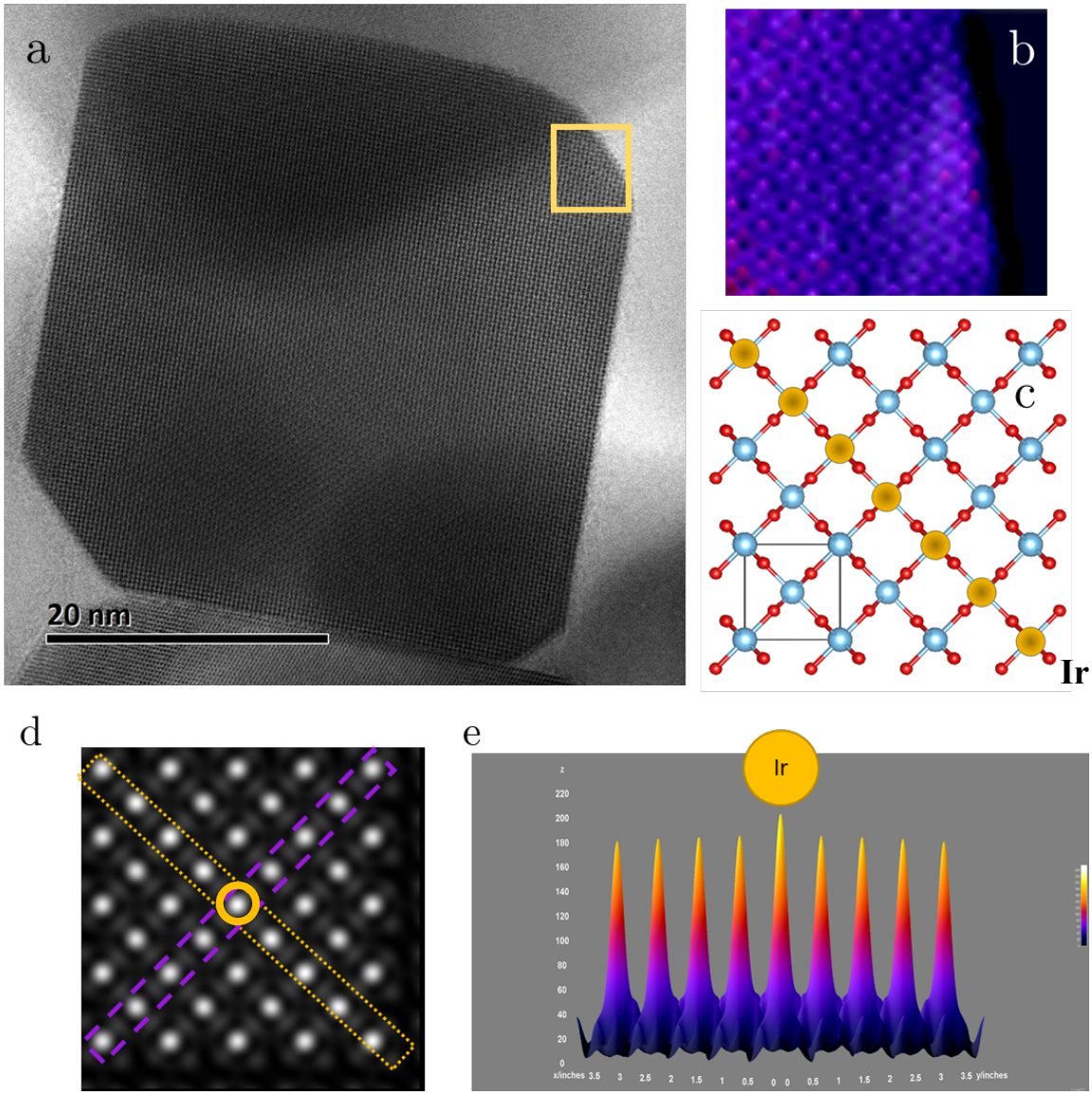

Figure 23 shows an HAADF-STEM image of Ir/TiO_2 in (a). In (b), a 3D plot of an ImageJ image is presented, depicting the corner of the crystal highlighted in yellow in the HAADF image in (a). In (c), there is an illustration of the crystal face when an entire column of Ti on the TiO_2 surface was intentionally modified in the diagonal, as shown. In (d), the SimulaTEM image with the iridium atoms modified as in the (c) image is displayed, along with a purple rectangle indicating the line plotted in the intensity profile in (e). In (e), we show where the iridium atom was positioned on the surface, with its intensity being lower compared to the other Ti columns.

It is evident that discerning the difference in intensities due to a single iridium atom on the surface of a TiO_2 crystal is physically challenging, primarily because of the

contribution of the titanium column signal within the crystal. Therefore, in the following micrographs, the brighter points observed are attributed to iridium.

Advanced AC-HAADF-STEM measurements were used to visually examine the distribution of Ir in the 0.25% Ir/TiO_2 DPU catalyst see **Figure 24**. Interestingly, no Ir nanoclusters were observed, and individual Ir atoms were identified as bright dots highlighted in yellow. These Ir atoms were consistently located on the Ti sites of the TiO_2 support. It is worth noting that these images were obtained without specifically orienting the crystal.

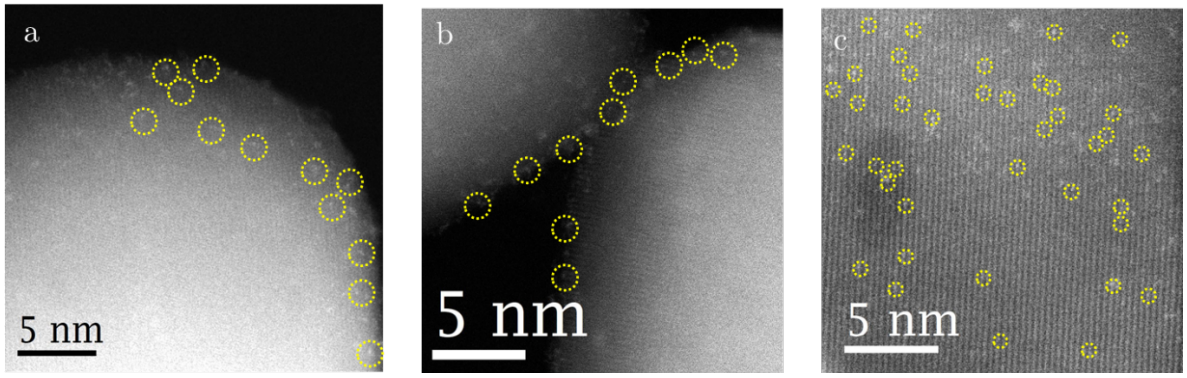

Figure 24. AC-HAADF-STEM measurements were employed to visually inspect the distribution of Ir in the 0.25% Ir/TiO_2 catalyst. Notably, no Ir nanoclusters were observed, and some individual Ir atoms were identified as bright dots highlighted in yellow circles.

Through StatSTEM, the surface of the Ir/TiO_2 system was analyzed. Since the iridium atoms are not oriented like a crystal of iridium, nor are they in all positions of Ti within the lattice, the analysis revealed a random distribution. When it comes to titanium, simulating multiple atoms at once is quite challenging. From micrograph in **Figure 25a**, data was filtered within StatSTEM, and the yellow area was selected. The program detects the positions and reports that we have columns of one and two atoms. Sometimes, iridium takes the positions of titanium in the lattice. The intensity profile clearly shows the more intense iridium atoms on the surface.

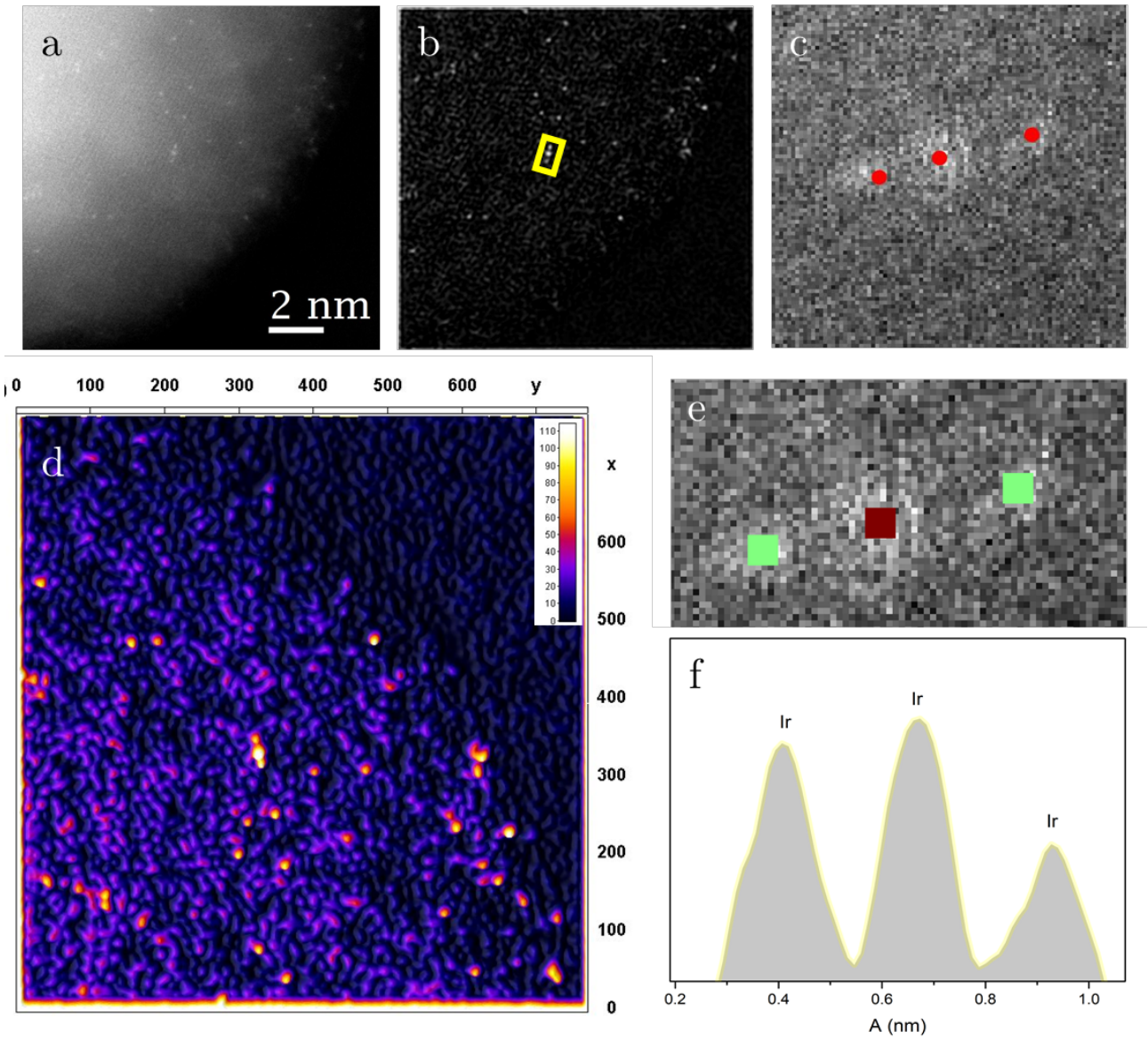

Figure 25: An Ir/TiO_2 HAADF micrograph is presented in (a), where in (b) we highlight the positions of isolated atoms using the peak finder option in StatSTEM. In the same image, a region containing apparently three atoms in a row is chosen and outlined in a yellow rectangle. StatSTEM in (c) displays the positions selected by the program when integrating the iridium parameters. Image (d) shows the 3D rendering of image (b) using ImageJ, where the brighter or yellowish positions stand out as individual iridium atoms due to their intensity compared to others on the surface. In (e), the atomic counting performed by STAT STEM is shown, with green indicating a single atom and red indicating two atoms. When plotted as an intensity profile in (f), similar heights are observed for one and two atoms. It is likely that we are observing a single atom per column; however, the crystal orientation may highlight two atoms due to the non-uniform surface, as observed in TiO_2.

Ir/TiO_2-Impregnation

In the case of Ir/TiO_2-Impregnation, a similar situation was observed. When aligning the crystals and obtaining well-oriented micrographs for the use of the StatSTEM tool, a significant challenge arose in distinguishing between iridium and titanium atoms. This was due contrast diffraction to the intensity shielding caused by the titanium columns compared to the presence of a single iridium atom on the crystal surface. Please refer to **Figure 26** for further details.

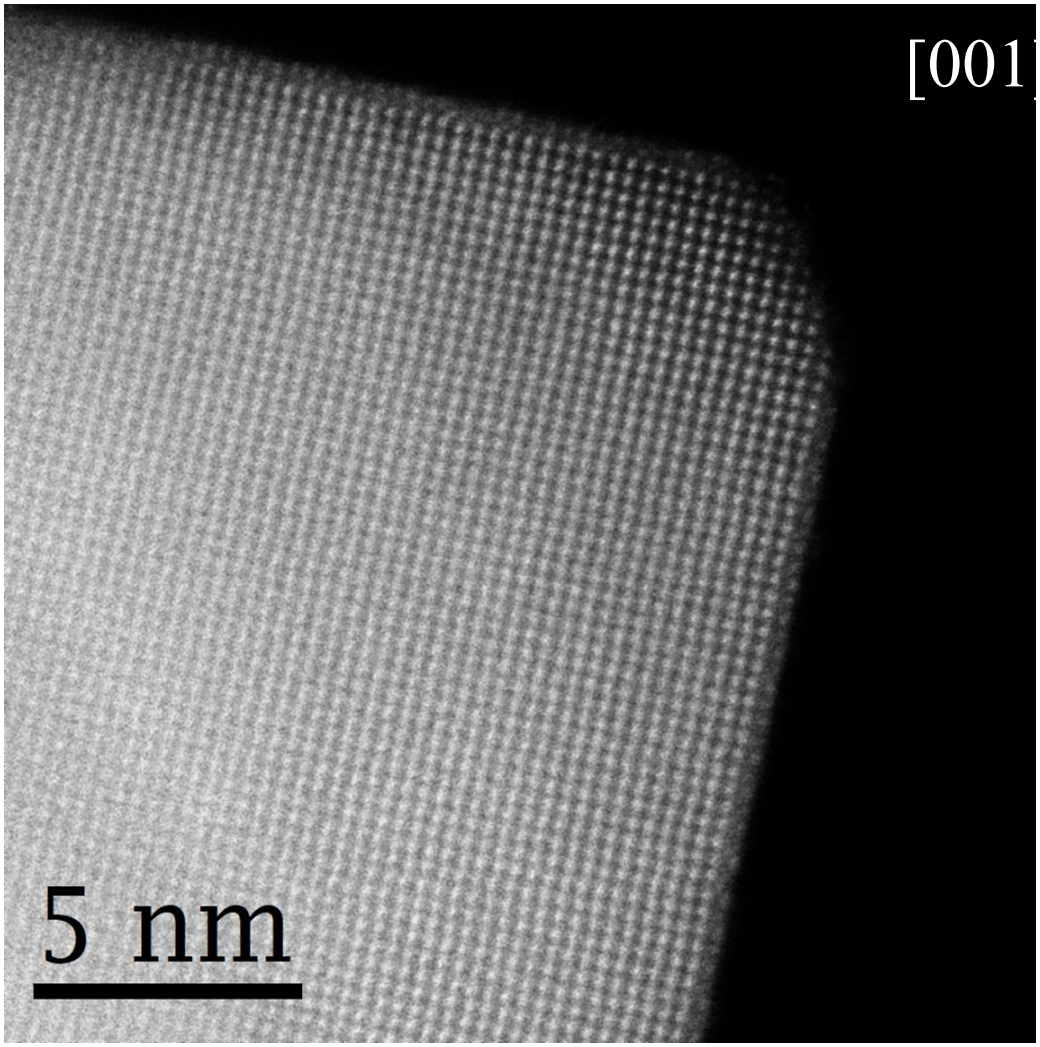

Figure 26. HAADF-STEM image of Ir/TiO_2-Impregnation.

However, when examining the system without specific orientation, micrographs are generated in which iridium atoms are highly dispersed on the material's surface. In **Figure 27** are shown in yellow circles Ir monodisperse on TiO_2 surface.

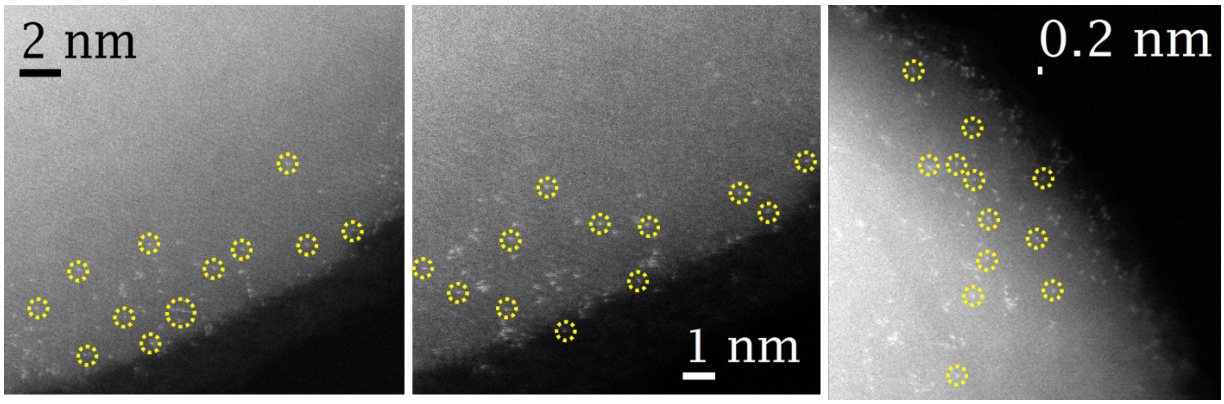

Figure 27. AC-HAADF-STEM measurements were employed to visually inspect the distribution of Ir in the 0.25% Ir/TiO_2-Impregnation catalyst. Individual Ir atoms were identified as bright dots highlighted in yellow.

Figure 28 displays the AC-HAADF-STEM micrograph of the Ir/TiO_2 synthesis carried out through impregnation. It is noteworthy to observe scattered iridium atoms on the support in **Figure 28a** there is a HAADF-STEM of the system. In **Figure (b),** the outcome of the filtering process performed by the StatSTEM system is presented, while in Figure **(c-d)**, the selected atoms for creating the model are outlined. In **Figure (e),** atomic quantification is depicted, with the green color representing a single iridium atom, and in red, two iridium atoms are counted. It is suggested that, on occasion, iridium occupies positions in the titanium lattice defects within the support. In **Figure (f-g)**, the 3D representation of the atom quantification model performed by StatSTEM is shown. The model appears to depict iridium atoms in close proximity, resembling a small one-dimensional iridium atom cluster. When examining the model in profile, the iridium atom contributing to the signal within the support can be observed. In **Figure (h-i)**, the distances between iridium atoms are analyzed. These iridium atoms do not form an iridium crystal

lattice, as their lattice parameters are dissimilar to those of iridium. Additionally, the micrographs are misaligned, suggesting that the issue isn't solely one atom sitting atop another, resulting in a double counting of atoms. Instead, this misalignment, possibly due to a slight tilt see **Figure 29 h**, could indicate the presence of an iridium atom situated further beneath the support. In summary, it can be concluded that these iridium atoms are randomly dispersed on the surface support.

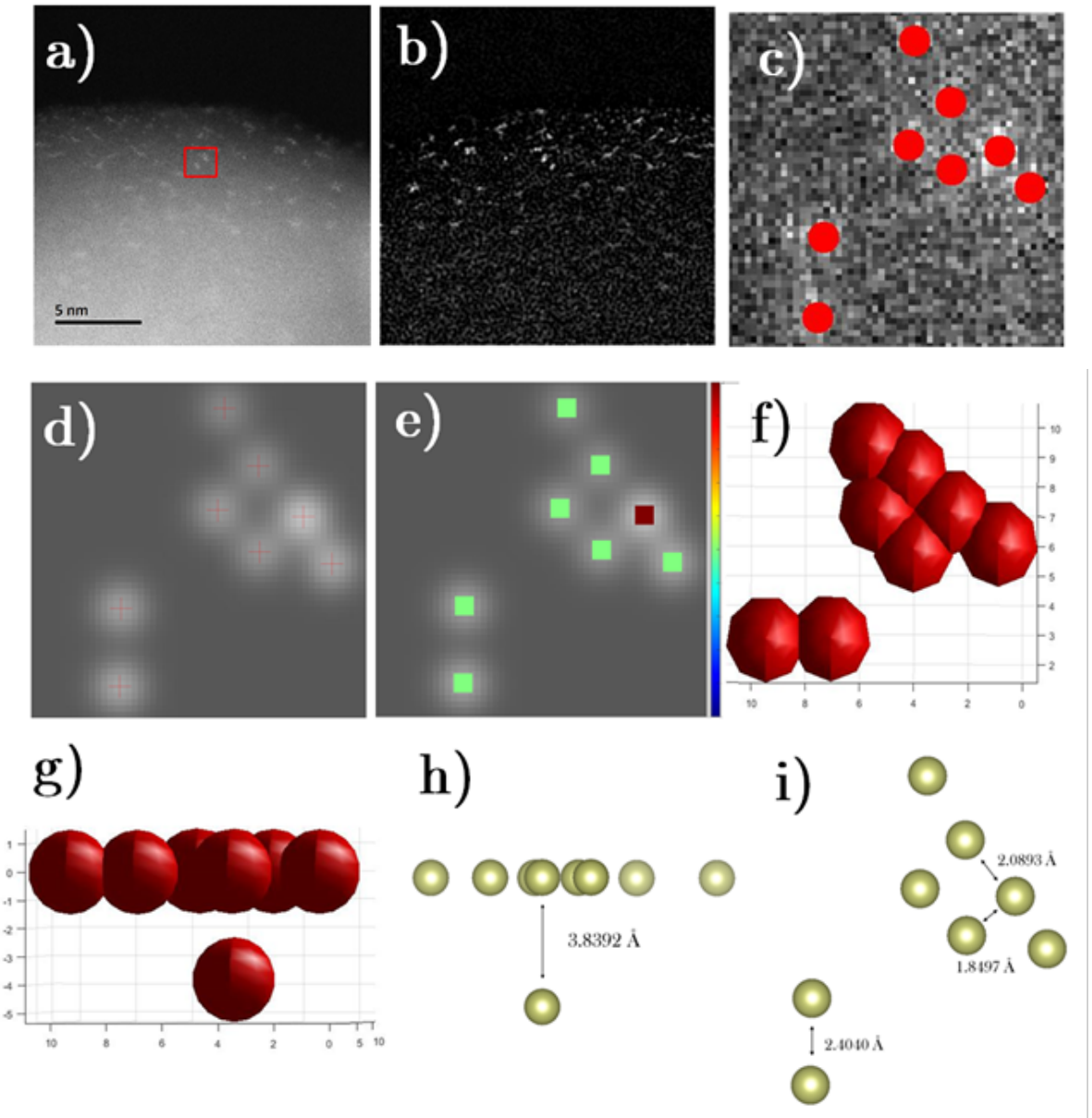

Figure 28. Ir/TiO_2-Impregnation A) HAADF-STEM image, B) image filtered using

StatSTEM, C-D) atom selection model, E) atom quantification, F-G) 3D model of surface iridium, H-I) measurements between iridium atoms dispersed on the support.

10.3 Reduction Properties

Presenting the TPR profiles of the Ir/TiO_2 systems; the hydrogen consumption with respect to temperature is observed. See TPR profiles in **Figure 29**.

For titanium oxide, from room temperature to 600 °C, there are virtually no signs of hydrogen consumption. However, a partial reduction of TiO_2 has been reported at 450 °C[74]. The reduction of TiO_2 is described at 600 °C[75], therefore only noise is observed. The small peak at 436 °C may be associated with the partial reduction of titanium.

The reduction of iridium oxide is characterized by hydrogen consumption with maxima located near 100°C for individual iridium particles. Complete oxidation of iridium at 400°C has been reported [76]. It is shown that the presence of iridium affects the reduction properties of TiO_2. It is known that IrO_2 species are reduced at 303°C,[77] Also, a peak was identified at 381°C assigned to the reduction of Ir species[77].

In Ir/TiO_2-DPU, peaks are observed at 123, 183, 227, 342, and 376°C primarily. It has been described that the peaks near 120°C are attributed to the transformation of IrO_2 to metallic Ir[78,79].

In the case of Ir/TiO_2-Impregnation, the peak located at 240°C is associated with IrOx species exhibiting weak and moderate interactions with the support[78].

In both systems there is plenty peaks between 144°C and 280°C that aren't described individually, nevertheless describe peaks between 150°C and 250°C as the reduction of IrOx to metallic iridium[80]. The peaks at 376°C and 377°C may be related to the reduction of Ir species[77]. In general, there is a change observed in the reduction profiles due to the presence of iridium.

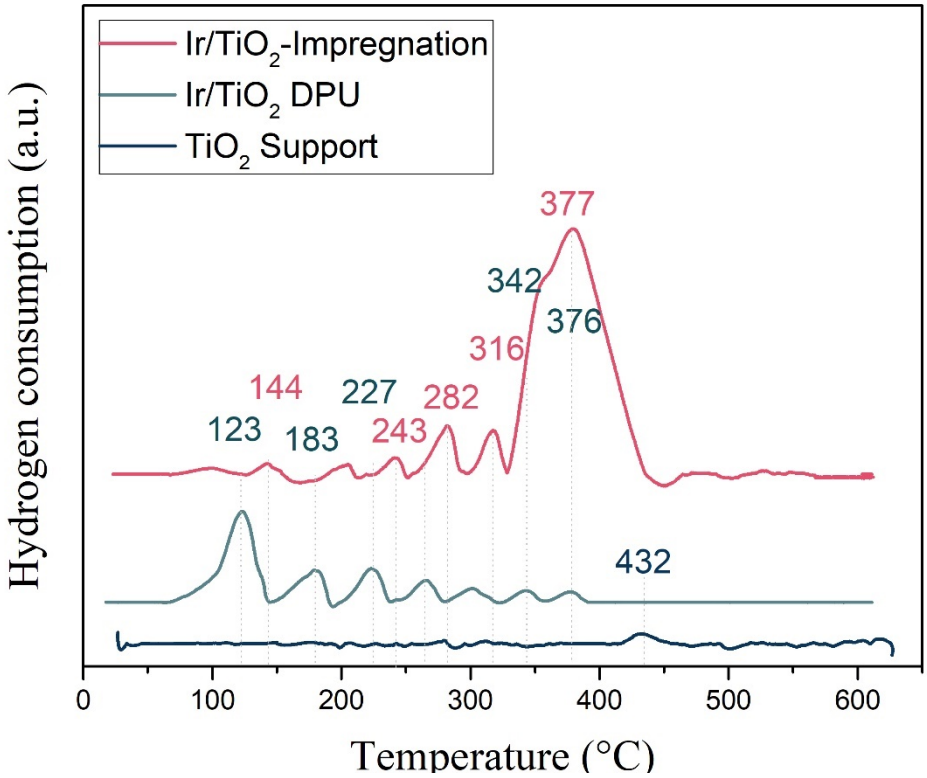

Figure 29. Profile reduction of temperature programmed reduction of A, M, and TiO_2.

We observe a reduction to a metallic state in the TPR of the sample synthesized by DPU, with no further changes after 376. In other words, the metallic state is achieved before 376. On the contrary, for $IrTiO_2$ synthesized by impregnation, multiple H2 consumptions are noted, suggesting the presence of Ir oxide in some fraction of the material.

10.4 X-ray photoelectron spectroscopy

XPS analysis of Ir/TiO_2-DPU and Ir/TiO_2-Impregnation revealed the characteristic peaks from the orbitals present in the samples. In **Figure 30 a-b** we can see the survey of the complete synthesis.

The binding energy was corrected based on the C1s peak observed at ~285. eV. The complete XPS spectrum of the systems is displayed. When selecting the spectrum in

the Multipack analysis software, signals are shown due to the presence of Ti, O, and Ir, in addition to the calibration peak, which is C 1s.

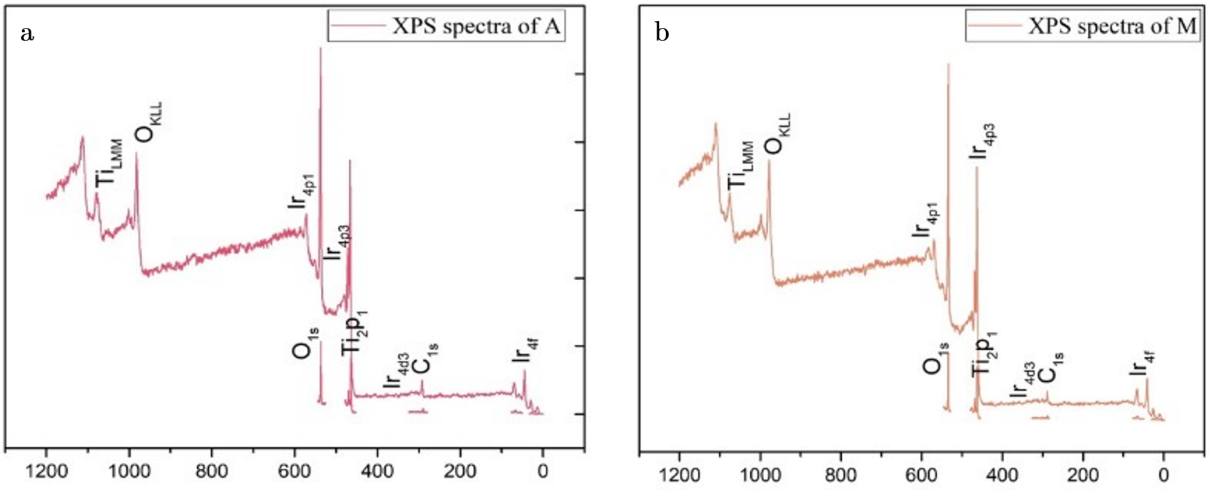

Figure 30. XPS survey in a) Ir/TiO_2-DPU and b)Ir/TiO_2-Impregnation

We work with a reference sample, the support. The pretreatment of been dried and reduced was applied to the TiO_2 support for analysis as a reference. The reference for Ir^0 and IrOx[63] was revised to compare whether the metallic state was present.

In **Figure 31** a-b displays the TiO_2 reference. In **Figure 31**c displays the Ir^0 reference from[63].

In Ir/TiO_2-DPU and Ir/TiO_2-Impregnation, the binding energies of O1s and Ti2p are depicted. It's noteworthy that the signal appears wider in certain areas. Evidence of a bond on the surface can be noticed compared to the reference in the oxygen and titanium regions. Since it does not correspond to the Ti 2p or O1s signals, and it also does not appear in the reference sample, there is suspicion of the existence of a bond between Ir and Ti. See Figure **31c-d** for Ir/TiO_2-DPU and **Figure 31g-h** for Ir/TiO_2-Impregnation.

In both samples, Ir_0 is observed in the 4f orbital. **Figure 31e** for Ir/TiO_2-DPU and **Figure 31i** for the Ir/TiO_2-Impregnation.

Note that the Ir (4f) region **Figure 31 e, i** overlaps with the Ti(3s) region of TiO_2. Therefore, fitting was accomplished using model spectra obtained from a treated TiO_2 sample, and the concentration of iridium was determined from the 4f peaks and compared with that derived from the equivalent (4d) peaks.

Due to the congruence in the crystallite structures of IrO_2 and rutile, the initial deposition of iridium onto rutile led the first iridium atoms to predominantly occupy positions corresponding to titanium atoms on the rutile crystallite surface. This preference was rooted in the greater stability of these sites for iridium atoms on this surface. Consequently, this substitution induced deformation in the original Ti-O-Ti-O local environment on the respective rutile face, resulting in a transformation into Ti-O-Ir-O.[81]

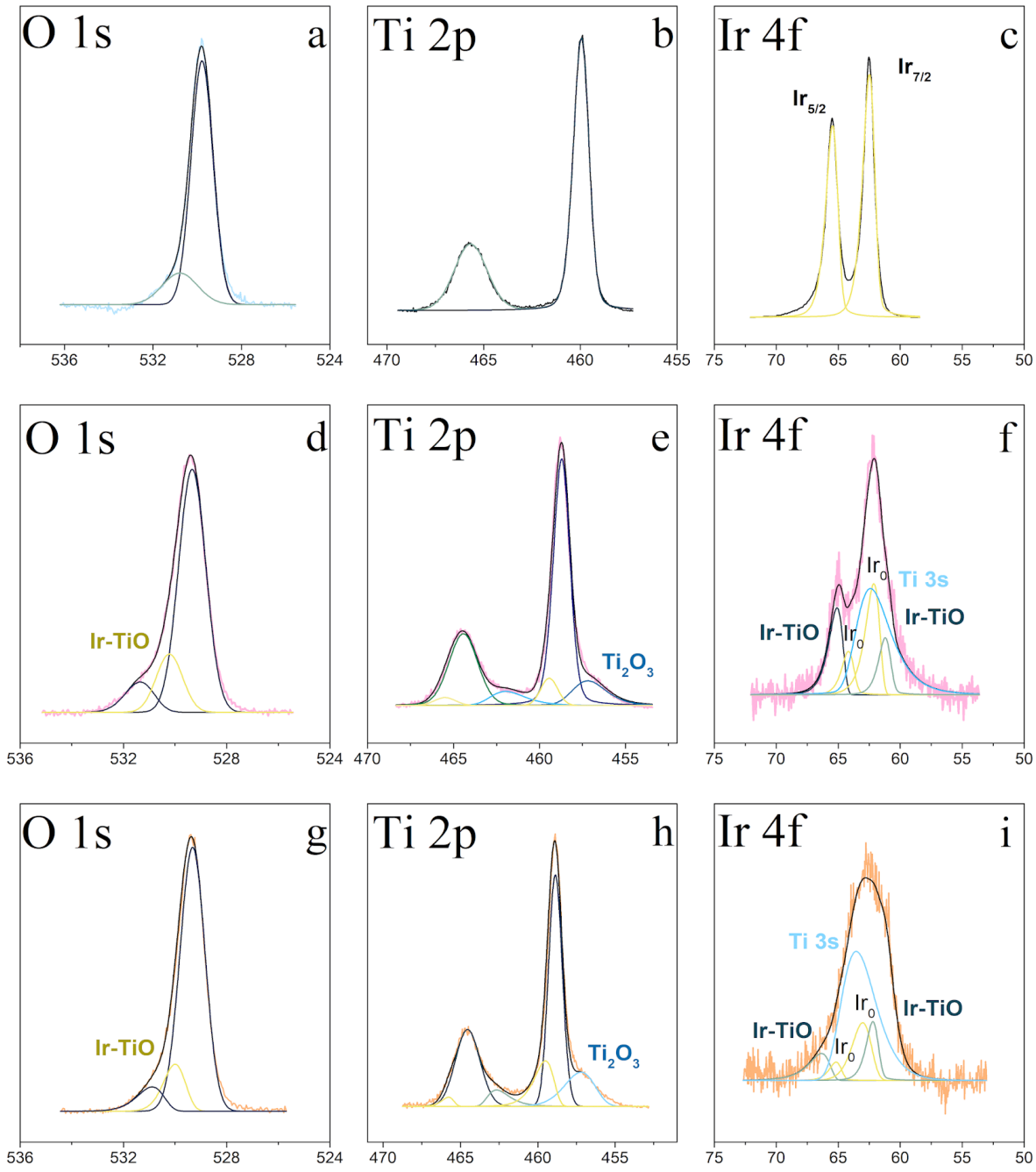

Figure 30. XPS of O1s for reference in a, for A sample in d, for M sample in g. Ti 2p orbital in reference in b, for A sample in e and for M sample in h. Ir 4f orbital from reference in c, for A sample in f and for M sample in i.

The binding energies for O1s, Ti2p, and Ir 4f are shown. Additionally, the atomic proportion of iridium in the metallic state and the proportion that is bonded with Ti are displayed. This display in the spectra can shown a superficial bonding from

Ir-TiO_2. The spectral parameters obtained by XPS for samples are summarized at Table 6.

Table 6 Binding energies of O1s, Ti2p and Ir4f

Sample	O 1s	Ti2p $_{3/2}$	Ir 4f
References TiO_2 and Ir	531.05 eV 529.39 eV	465.58 eV 459.98 eV	65.45 eV 62.44 eV
0.25% Ir/TiO_2-DPU	531.35eV 529.34eV	464.43eV 458.70eV	64.18eV 61.21eV
0.25% Ir/TiO_2-Imp	530.89eV 429.89eV	464.43eV 458.70eV	65.18eV 62.21eV

For the reference of calcined TiO_2 at 100°C, binding energies of 529.39 eV and 531.05 eV were obtained for the satellite in the O 1s orbital, and for Ti 2p, values of 465.58 eV and 459.98 eV were obtained, indicating the contribution of Ti_2O_3. For metallic Iridium 4f, binding energies of 65.45 eV and 62.44 eV were observed.

In the sample synthesized by DPU, O 1s exhibits essentially the same binding energy values. However, there is a contribution related to the interaction of Iridium. In the Ti 2p section, changes in binding energy are observed due to the presence of Iridium, with an overlap of the Iridium signal within the 2p orbitals. The presence of Ti_2O_3 is evident. The Iridium orbital shows binding energies of 64.18 eV and 61.21 eV, which are slightly lower due to the interaction with Titania oxide.

For the sample prepared through Impregnation, O 1s displays binding energies of 530.89 eV and 429.89 eV, slightly lower than the reference. In Figure 32, a contribution is shown due to the interaction of Iridium with the surface. In the Ti 2p orbitals, binding energies of 464.43 eV and 458.70 eV are slightly lower than the reference due to the presence of Iridium. In the 4f orbital, binding energies of 65.18 eV and 62.21 eV are presented.

According to the results obtained in TPR, for sample A, the total reduction of iridium to the metallic state was achieved earlier. However, for sample M, several peaks are observed that cannot be fully identified. Through XPS on sample M, a sum of the spectra shows the presence of iridium 0. Nevertheless, we do not rule out the presence of other iridium species.

10.5 Quantification

Ir/TiO_2 (A) was obtained from $IrCl_3$, and it has been reported that chlorine can reduce the catalytic activity of the systems. To counteract this effect, washes were carried out to remove the chlorine present in the samples. Therefore, it was expected that the actual deposited amount would be less than the theoretical one.

Ir/TiO_2-Impregnation (M) sample was prepared using a stock solution prepared in the laboratory. From the outset, this sample proved to be more accessible for characterization in terms of the presence of iridium.

As is shown in Table 7, an attempt was made to roughly quantify the amount of supported metal using semi-quantitative techniques and quantitative techniques. However, no signals related to iridium could be detected through EDS. This may be due to the fact that the nominal theoretical amount is at the limit of resolution, and, as expected, the deposited metal amount turned out to be lower.

Table 7 Quantification of iridium supported in TiO_2

Characterization Technique	Composition of Ir in synthesis A	Composition of Ir in synthesis M
EDS	-	-
ICP	0.1552 mg/kg	0.3282 mg/kg
XPS	0.6%	0.4%

To determine the actual supported amount, ICP-Ms was used. In the case of the Ir/TiO_2-DPU sample, the amount was less than expected, possibly due to washes performed during the synthesis. For the Ir/TiO_2-Impregnation system, a slightly higher amount was obtained than expected. It is estimated that the concentration of the stock solution might account for this difference, although the nominal amount remains quite low compared to what has been reported regarding single-atom catalyst (SAC) systems.

10.6 CO Adsorption followed by Diffuse Reflectance

DRIFT spectra were performed on samples obtained by deposition-precipitation with iridium deposited on the surface as nanoparticles and isolated atoms. Additionally, synthesis was carried out by impregnation with monodisperse atoms.

The comparison between the systems shows that when iridium is deposited in the form of nanoparticles (Synthesis B from Table 3), an asymmetric adsorption band with a maximum at 2056 cm^{-1} is obtained, notably wide. This breadth could be related to the presence of different iridium species on the support, not only due to the existence of monoatomic iridium sites. The systems studied in this work, on the other hand, both exhibit their maximum adsorption band at 2070 cm^{-1}, a characteristic of isolated iridium atoms. It is important to note that, despite being

reported previously, the band originating solely from individual iridium atoms had not been clearly defined due to the signal from other iridium species. See **Figure 31**.

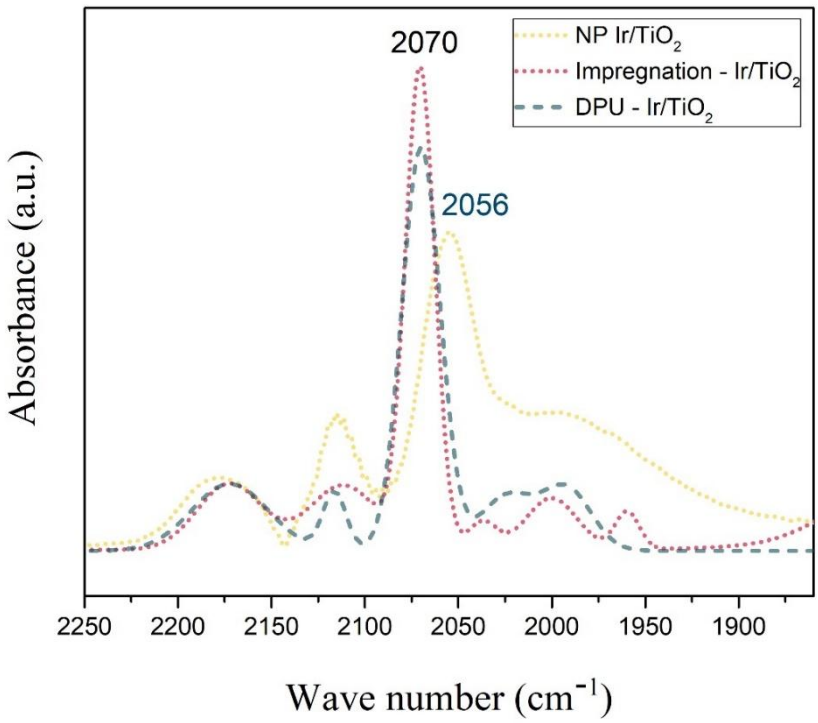

Figure 31. DRIFT Spectra of Ir/TiO_2 samples with NPs and single atoms supported on TiO_2.

Ir/TiO_2-DPU

For Ir/TiO_2 in **Figure 32** prepared by deposition-precipitation, the contribution of six bands at 2173, 2112, 2070, 2036, 1998, and 1968 cm^{-1} was revealed. It has been described that the band located at 2173 could be assigned to CO adsorbed on TiO_2. [70,82]In the case of 2112 to the symmetric and antisymmetric modes, respectively, of $Ir/(CO)_2$ dicarbonyl species. The bands located to 2070 cm^{-1} and 1998 cm^{-1} could be assigned to the symmetric and asymmetric vibrations of Ir gem dicarbonyl (Ir(CO)2L, where L is the support [83,84] . The 2070 cm^{-1} it's also known as the mononuclear band of Ir0 -CO, where the o gem dicarbonyl CO (GCO) species on Ir^+

sites.[85,86] The band at ca. 1968 cm^{-1} could be assigned to bridge adsorbed CO (BCO) on supported Ir^0 sites.

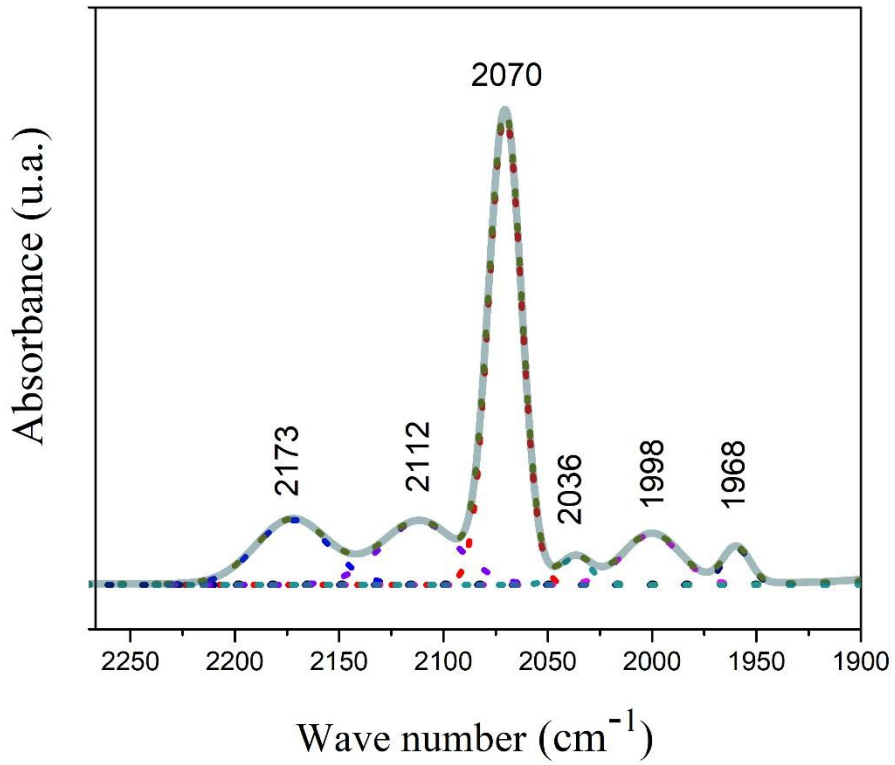

Figure 32. DRIFT spectra of Ir/TiO_2-DPU.

Ir/TiO_2-Impregnation

In Ir/TiO_2 prepared by impregnation see **Figure 33**, the contribution of five bands at 2173, 2116, 2070, 2026, and 1992 cm^{-1} was revealed. The first one could be described as CO adsorbed on TiO_2. The 2112 band could be referred to as the symmetric and antisymmetric modes, respectively, of $Ir/(CO)_2$ dicarbonyl species. The bands located at 2070 cm^{-1} and 1992 cm^{-1} could be assigned to the symmetric and asymmetric vibrations of Ir gem dicarbonyl (Ir(CO)2-Support). Additionally, you can observe the 2070 cm^{-1} mononuclear band of Ir0 -CO, where the gem dicarbonyl CO (GCO) species are on Irδ+ sites. The band at approximately 1962 cm^{-1} could be assigned to bridge-adsorbed CO (BCO) on supported Ir^0. One challenge

in the DRIFT results analysis is that there are bands located at various wave numbers contributing to the same signal.

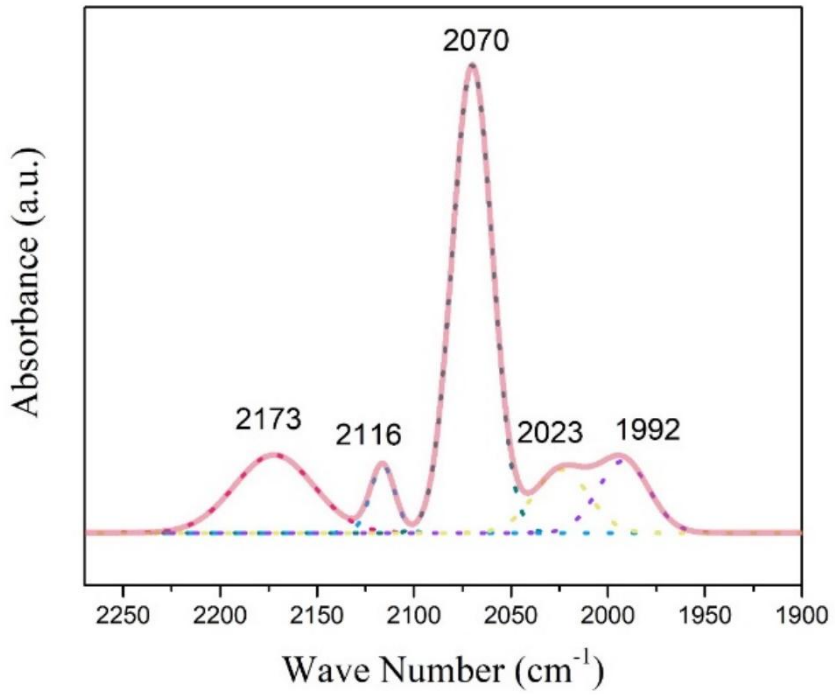

Figure 33. DRIFT spectra of Ir/TiO_2 -Impregnation.

10.6 Catalytic Reactivity

We have the syntheses conducted in this study, where CO conversion as a function of reaction temperature in the CO oxidation process was examined for Ir/TiO_2 catalysts prepared using the Deposition-Precipitation and impregnation methods, with a nominal iridium concentration of 0.25%. These samples underwent direct reduction at 300°C, see **Figure 34**.

In the case of the Ir/TiO_2-DPU sample, its catalytic activity commenced at 82 degrees Celsius, and from 92 degrees onwards, it exhibited an exponential increase, reaching its peak at 186 degrees, where CO conversion was most prominent, and concluding at 247 degrees. Conversely, for the Ir/TiO_2-Imp sample, CO oxidation

began at a lower temperature of 54 degrees, and from that point onward, the CO conversion curve displayed exponential growth. At 180 degrees, it achieved a higher proportion of CO conversion, ultimately concluding at 200 degrees. In general, the impregnation-prepared synthesis demonstrated activity at lower temperatures compared to the DPU-synthesized sample. A total of 40 mg of material was utilized for these tests. At 173°C, the T 50 is observed for impregnation, and at 191°C for DPU.

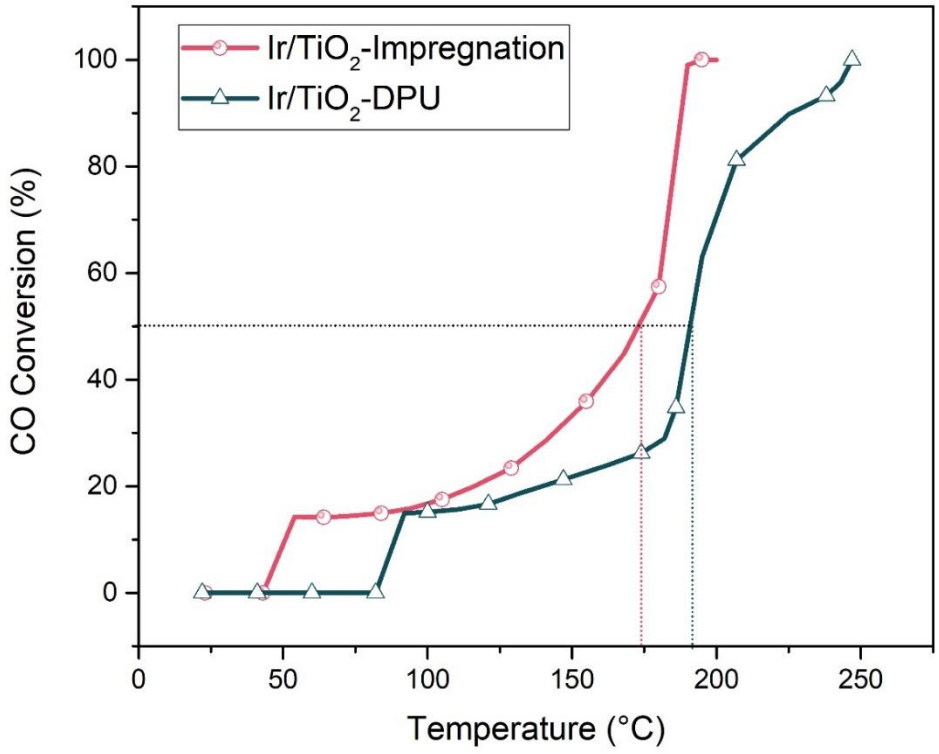

Figure 34. CO conversion with catalysts Ir/TiO_2-DPU and Ir/TiO_2-Impregnation activated in hydrogen.

The catalysts in **Figure 34** exhibit their catalytic potential by initiating the CO oxidation reaction at a low temperature of 50°C, achieving complete conversion at temperatures exceeding 200 °C. The orange sample determined that these catalysts contained 2.2 wt.% of iridium, despite a nominal concentration target of 4 %wt.

Irrespective of the activation temperature, all these catalysts demonstrated their ability to catalyze CO oxidation, with remarkable conversion rates observed at temperatures beyond 200°C. The CO conversion reaction was executed utilizing one gram of the sample.

The **Figure 35** illustrates the CO conversion rates as a function of reaction temperature during CO oxidation for Ir/TiO_2 samples. These samples encompass one that underwent calcination (depicted in red) and another that was subjected to reduction in H_2 (depicted in black). Evidently, neither of these samples exhibits activity at room temperature, as the light-off temperature surpasses 250°C. Interestingly, the orange Ir/TiO_2 sample, having undergone reduction in H2, presents slightly elevated activity compared to the calcined sample. Cortes et al. have previously reported that the Ir/TiO_2 catalyst tends to exhibit nearly zero activity, particularly at temperatures below 150°C. This experimental reaction employed 0.02 grams of the sample.

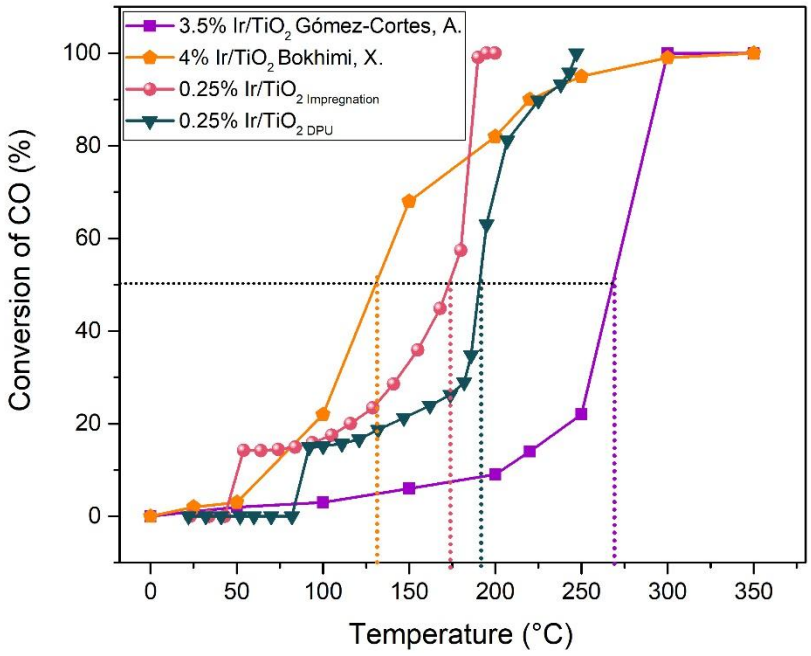

Figure 35. CO references with the catalyst of study in this work.

When compared to similar reported systems, a notably higher catalytic activity is evident in our samples, with CO conversion initiating earlier and concluding at lower temperatures. Furthermore, it is noteworthy that these catalysts exhibit a lower iridium content on their respective supports. In the case of Ir/TiO_2-DPU (A), the actual iridium concentration is 0.1552 %wt, whereas in Ir/TiO_2-Impregnation (M), it amounts to 0.3282 %wt. These values are notably less than what has been reported for dispersed atom systems. This demonstrates that monodisperse iridium catalysts supported on titanium oxide are highly effective for CO conversion and are considerably better than nanoparticle based systems.

As a perspective of the work, it would be important to analyze how many cycles it remains active, how its catalytic activity decreases, and whether it continues to be a SAC. It is crucial to mention that SACs lack stability; therefore, finding an alternative to this challenge is essential. To continue with this project, stabilization by ionic liquids at the Ir sites is proposed.

11. Conclusion

In summary, our findings confirm that it is entirely feasible to deposit iridium atoms onto supports using the deposition-precipitation and simple impregnation methods, provided that the nominal iridium concentration is 0.25%. The proper reduction at 300°C in a hydrogen atmosphere, as evidenced by TPR, supports the remarkable dispersion of iridium atoms, as demonstrated in the HAADF-STEM and DRIFT images. Additionally, DRIFT analysis highlights the high activity in CO adsorption on single Ir sites, with similar adsorption bands in both synthesis methods.

XPS analysis reveals the presence of a Ti-Ir bond on the sample's surface, along with iridium in metallic form. Using ICP-MS, we confirmed the actual iridium content. The synthesized materials have 0.1552 and 0.3282 mg/kg, which constitutes a remarkably low. The reactivity of these systems were confirmed through CO oxidation, displaying activity at temperatures below 150°C, surpassing catalysts with similar characteristics with 10-15% of the metal that has been used in NPs systems. Furthermore, our study emphasizes the promising prospect of utilizing TiO_2 as a support for iridium, a strategy that has received less attention in previous research. The strong metal-support interaction (SMSI) between TiO2 and iridium contributes to the effective dispersion of iridium atoms as isolated species, a highly desirable attribute in catalytic applications. The exceptional catalytic activity of iridium further enhances the overall system's performance by making efficient use of all available iridium atoms, thereby improving atomic efficiency.

These results open new avenues for research and development of highly efficient and sustainable catalysts in key applications, underscoring the importance of thoroughly exploring the potential of TiO_2 as a support for iridium in future scientific and technological studies.

12. Annexes

12.1 Research outcomes

Molina-Torres M, Hernández-Cristóbal O and Mendoza-Cruz R (2023), *Small but mighty: unlocking the catalytic power of individual iridium atoms on titanium oxide.* Front. Nanotechnol. 5:1257240. doi: 10.3389/fnano.2023.1257240

13 References

1. De Vries, J. G. et. al. Homogeneous and heterogeneous catalysis in the industry. **1**, (2012).
2. Yang, X.-F. *et al.* Single-Atom Catalysts: A New Frontier in Heterogeneous Catalysis. *Acc Chem Res* **46**, 1740–1748 (2013).
3. Herzing, A., Kiely, C., Carley, A., Landon, P. & Hutchings, G. Identification of Active Gold Nanoclusters on Iron Oxide Supports for CO Oxidation. *Science* **321**, 1331–1335 (2008).
4. Turner, M. *et al.* Selective oxidation with dioxygen by gold nanoparticle catalysts derived from 55-atom clusters. *Nature* **454**, 981–983 (2008).
5. Remediakis, I. N., Lopez, N. & Nørskov, J. K. CO Oxidation on Rutile-Supported Au Nanoparticles. *Angewandte Chemie International Edition* **44**, 1824–1826 (2005).
6. Lin, J. *et al.* Design of a Highly Active Ir/Fe(OH)x Catalyst: Versatile Application of Pt-Group Metals for the Preferential Oxidation of Carbon Monoxide. *Angewandte Chemie* **124**, (2012).
7. Fu, J. *et al.* Synergistic Effects for Enhanced Catalysis in a Dual Single-Atom Catalyst. *ACS Catal* **11**, 1952–1961 (2021).
8. Lei, Z. *et al.* Coordination modulation of iridium single-atom catalyst maximizing water oxidation activity. *Nat Commun* **13**, (2022).
9. Uzun, A., Ortalan, V., Browning, N. D. & Gates, B. C. A site-isolated mononuclear iridium complex catalyst supported on MgO: Characterization by spectroscopy and aberration-corrected scanning transmission electron microscopy. *J Catal* **269**, 318–328 (2010).
10. Xiao, M. *et al.* A Single-Atom Iridium Heterogeneous Catalyst in Oxygen Reduction Reaction. *Angewandte Chemie International Edition* **58**, 9640–9645 (2019).
11. kottwitz2021.
12. Zhou, Y., Wang, Z. & Liu, C. Perspective on CO oxidation over Pd-based catalysts. *Catal Sci Technol* **5**, 69–81 (2015).
13. Uzun, A., Ortalan, V., Browning, N. D. & Gates, B. C. A site-isolated mononuclear iridium complex catalyst supported on MgO: Characterization by spectroscopy and aberration-corrected scanning transmission electron microscopy. *J Catal* **269**, 318–328 (2010).
14. Monteseguro, V. *et al.* Phase stability and electronic structure of iridium metal at the megabar range. *Sci Rep* **9**, (2019).
15. Li, J., Liu, J. & Zhang, T. Remarkable Performance of Ir 1 /FeO. *J Am Chem Soc* **135**, 15314–15317 (2013).
16. Cao, W. *et al.* In-situ synthesis of single-atom Ir by utilizing metal-organic frameworks: An acid-resistant catalyst for hydrogenation of levulinic acid to γ-valerolactone. *J Catal* **373**, 161–172 (2019).
17. Cao, W. *et al.* In-situ synthesis of single-atom Ir by utilizing metal-organic frameworks: An acid-resistant catalyst for hydrogenation of levulinic acid to Γ-valerolactone. *J Catal* **373**, 161–172 (2019).
18. Lin, J. *et al.* Remarkable Performance of Ir1/FeOx Single-Atom Catalyst in Water Gas Shift Reaction. *J Am Chem Soc* **135**, 15314–15317 (2013).
19. Lu, Y. *et al.* Identification of the active complex for CO oxidation over single-atom Ir-on-MgAl2O4 catalysts. *Nat Catal* **2**, (2019).
20. Li, Z. *et al.* Iridium single-atom catalyst on nitrogen-doped carbon for formic acid oxidation synthesized using a general host–guest strategy. *Nat Chem* **12**, 1–9 (2020).
21. Wang, Y. *et al.* Single–atom Ir1 supported on rutile TiO2 for excellent selective catalytic oxidation of ammonia. *J Hazard Mater* **432**, 128670 (2022).
22. Shao, X. *et al.* Iridium Single-Atom Catalyst Performing a Quasi-homogeneous Hydrogenation Transformation of CO2 to Formate. *Chem* **5**, 693–705 (2019).
23. Zhao, J. *et al.* A heterogeneous iridium single-atom-site catalyst for highly regioselective carbenoid O–H bond insertion. *Nat Catal* **4**, 523–531 (2021).
24. Cao, W. *et al.* In-situ synthesis of single-atom Ir by utilizing metal-organic frameworks: An acid-resistant catalyst for hydrogenation of levulinic acid to Γ-valerolactone. *J Catal* **373**, 161–172 (2019).
25. Zhu, Y. *et al.* Iridium single atoms incorporated in Co3O4 efficiently catalyze the oxygen evolution in acidic conditions. *Nat Commun* **13**, (2022).

26. Shan, J. *et al.* Short-Range Ordered Iridium Single Atoms Integrated into Cobalt Oxide Spinel Structure for Highly Efficient Electrocatalytic Water Oxidation. *J Am Chem Soc* **143**, 5201–5211 (2021).
27. wang2020.
28. Xia, C. *et al.* General synthesis of single-atom catalysts with high metal loading using graphene quantum dots. *Nat Chem* **13**, 887–894 (2021).
29. Chen, F., Jiang, X., Zhang, L., Lang, R. & Qiao, B. Single-atom catalysis: Bridging the homo- and heterogeneous catalysis. *Cuihua Xuebao/Chinese Journal of Catalysis* **39**, 893–898 (2018).
30. Pham, H. Q., Pham, H. T. Q., Huynh, Q. & Huynh, T. T. Single-Atom Iridium-Based Catalysts: Synthesis Strategies and Electro(Photo)-Catalytic Applications for Renewable Energy Conversion and Storage. *Coordination Chemistry Reviews* vol. 486 Preprint at https://doi.org/10.1016/j.ccr.2023.215143 (2023).
31. Molina-Torres, M., Hernández-Cristóbal, O. & Mendoza-Cruz, R. *Small but Mighty: Unlocking the Catalytic Power of Individual Iridium Atoms on Titanium Oxide I n r e v i e w.* www.frontiersin.org.
32. Zanella, R., Delannoy, L. & Louis, C. Mechanism of deposition of gold precursors onto TiO2 during the preparation by cation adsorption and deposition-precipitation with NaOH and urea. in *Applied Catalysis A: General* vol. 291 62–72 (2005).
33. Gómez-Cortés, A. *et al.* Au-ir/tio 2 prepared by deposition precipitation with urea: improved activity and stability in co oxidation. *Journal of Physical Chemistry C* **113**, 9710–9720 (2009).
34. Haruta, M. *Size-and support-dependency in the catalysis of gold.* (1997).
35. Milone, C., Trapani, M., Zanella, R., Piperopolulos, E. & Galvagno, S. Deposition-precipitation with Urea to prepare Au/Mg(OH)2 catalysts: Influence of the preparation conditions on metal size and load. *Mater Res Bull* **45**, 1925–1933 (2010).
36. Qin, H., Tan, X., Huang, W., Jiang, J. & Jiang, H. Application of urea precipitation method in preparation of advanced ceramic powders. *Ceramics International* vol. 41 11598–11604 Preprint at https://doi.org/10.1016/j.ceramint.2015.06.032 (2015).
37. Van Dillen, A. J., Terörde, R. J. A. M., Lensveld, D. J., Geus, J. W. & De Jong, K. P. Synthesis of supported catalysts by impregnation and drying using aqueous chelated metal complexes. in *Journal of Catalysis* vol. 216 257–264 (Academic Press Inc., 2003).
38. Ramos-Delgado, N. A., Gracia-Pinilla, M., Mangalaraja, R. V., O'Shea, K. & Dionysiou, D. D. Industrial synthesis and characterization of nanophotocatalysts materials: titania. *Nanotechnology Reviews* vol. 5 467–479 Preprint at https://doi.org/10.1515/ntrev-2016-0007 (2016).
39. Kominami, H. *et al.* Novel synthesis of microcrystalline titanium(IV) oxide having high thermal stability and ultra-high photocatalytic activity: thermal decomposition of titanium(IV) alkoxide in organic solvents. *Catal Letters* **46**, 235–240 (1997).
40. Scirè, S., Fiorenza, R., Bellardita, M. & Palmisano, L. Catalytic applications of TiO2. in *Titanium Dioxide (Tio$_2$) and Its Applications* 637–679 (Elsevier, 2021). doi:10.1016/b978-0-12-819960-2.00006-7.
41. Palcheva, R., Dimitrov, L., Tyuliev, G., Spojakina, A. & Jiratova, K. TiO 2 nanotubes supported NiW hydrodesulphurization catalysts: Characterization and activity. *Appl Surf Sci* **265**, 309–316 (2013).
42. J Tauster, S., C Fung, S., Baker, R. & A Horsley, J. *Strong Interactions in Supported-Metal Catalysts. Science (New York, N.Y.)* vol. 211 (1981).
43. Kim, A. Y. *et al.* CO2 methanation on Ru/TiO2 catalysts: on the effect of mixing anatase and rutile TiO2 supports. *Applied Catalysis B-environmental* **220**, 615–625 (2018).
44. Waseda, Y., Matsubara, E. & Shinoda, K. *X-Ray Diffraction Crystallography X-Ray Diffraction Crystallography Introduction, Examples and Solved Problems.*
45. Cohen, J. B. *X-ray diffraction studies of catalysts. Ultramicroseopy* vol. 34 (1990).
46. Kittel, C. *Introduction to Solid State Physics.* (John Wiley & Sons, Inc, 1967).
47. Sprague, M. J. Characterization of heterogeneous catalysts (Chemical industries series, Vol. 15). Herausgeg. von F. Delannay. Marcel Dekker, Inc., New York 1984. X, 409 S., zahlr. Abb. u. Tab., geb., SFr. 185,–. *Chemie Ingenieur Technik* **57**, 430 (1985).
48. Imelik, B. & Védrine, J. C. Catalyst Characterization: Physical Techniques For Solid Materials. in (2013).

49. Robert J. Keyse. *Introduction to Scanning Transmission Electron Microscopy (Microscopy Handbooks).* (Bios Scientific Pub Ltd; 1st edition, 1998).
50. CambridgeCore_CitationExport_12Oct2023.
51. Pennycook, S. J. , & N. P. D. *Scanning transmission electron microscopy: imaging and analysis.* (Springer Science & Business Media, 2011).
52. Williams, D. & Carter, C. *Transmission Electron Microscopy: A Textbook for Materials Science. Transmission electron microscopy. A textbook for materials science* vol. III (2009).
53. Plascencia, G., Mendoza-Cruz, R., Bazán-Díaz, L. & Yacaman, M. Gold Nanoclusters, Gold Nanoparticles, and Analytical Techniques for Their Characterization. in *Methods in molecular biology (Clifton, N.J.)* vol. 2118 351–382 (2020).
54. Hartel, P., Rose, H. & Dinges, C. Conditions and reasons for incoherent imaging in STEM. *Ultramicroscopy* **63**, 93–114 (1996).
55. Singhal, A., Yang, J. C. & Gibson, J. M. STEM-based mass spectroscopy of supported Re clusters. *Ultramicroscopy* **67**, 191–206 (1997).
56. Van Aert, S. *et al.* Quantitative atomic resolution mapping using high-angle annular dark field scanning transmission electron microscopy. *Ultramicroscopy* **109**, 1236–1244 (2009).
57. Singhal, A., Yang, J. C. & Gibson, J. M. STEM-based mass spectroscopy of supported Re clusters. *Ultramicroscopy* **67**, 191–206 (1997).
58. Kundu, P., Turner, S., Van Aert, S., Ravishankar, N. & Van Tendeloo, G. Atomic structure of quantum gold nanowires: Quantification of the lattice strain. *ACS Nano* **8**, 599–606 (2014).
59. De Backer, A. *et al.* Dose limited reliability of quantitative annular dark field scanning transmission electron microscopy for nano-particle atom-counting. *Ultramicroscopy* **151**, 56–61 (2015).
60. Fierro, J. L. G. *Spectroscopic characterization of heterogeneous catalysts.* (Elsevier, 1990).
61. Kottwitz, M., Li, Y., Wang, H., Frenkel, A. I. & Nuzzo, R. G. Single Atom Catalysts: A Review of Characterization Methods. *Chemistry–Methods* **1**, 278–294 (2021).
62. Bazin, P., Saur, O., Lavalley, J. C., Daturi, M. & Blanchard, G. FT-IR study of CO adsorption on Pt/CeO2: characterisation and structural rearrangement of small Pt particles. *Phys. Chem. Chem. Phys.* **7**, 187–194 (2005).
63. Jolm F. Moulder William F. Stickle Peter E.'Sobol Kennetlf D. Bomben. *Handbook of X-ray Photoelectron Spectroscopy.* (Perkin-Elmer Corporation, 1992).
64. John F. Watts, J. W. *An Introduction to Surface Analysis by XPS and AES.* (John Wiley & Sons, Ltd, 2003).
65. Stevie, F. A. & Donley, C. L. Introduction to x-ray photoelectron spectroscopy. *Journal of Vacuum Science & Technology A: Vacuum, Surfaces, and Films* **38**, (2020).
66. L. M. Blumberg. *Temperature-Programmed Gas Chromatography.* (Wiley-VCH, 2010).
67. Dal Nogare, Stephen. & Langlois, W. E. Programmed Temperature Gas Chromatography. *Anal Chem* **32**, 767–770 (1960).
68. Dr Saurabh Arora. Introduction to Gas Chromatography. *Auriga Research Ltd* (2014).
69. Gómez-Cortés, A. *et al.* Au-ir/tio 2 prepared by deposition precipitation with urea: improved activity and stability in co oxidation. *Journal of Physical Chemistry C* **113**, 9710–9720 (2009).
70. Haruta, M. *Size-and support-dependency in the catalysis of gold.* (1997).
71. Siang, J.-Y. *et al.* Hydrogen production from steam reforming of ethanol using a ceria-supported iridium catalyst: Effect of different ceria supports. *Int J Hydrogen Energy* **35**, 3456–3462 (2010).
72. Pellegrino, F., Sordello, F., Minella, M., Minero, C. & Maurino, V. The role of surface texture on the photocatalytic H2 production on TiO2. *Catalysts* vol. 9 Preprint at https://doi.org/10.3390/catal9010032 (2019).
73. Jiang, F. *et al.* First-principles atomistic Wulff constructions for an equilibrium rutile TiO 2 shape modeling. *Appl Surf Sci* **436**, 989–994 (2018).
74. Hernandez-Mejia, C. *et al.* Ru/TiO2-catalysed hydrogenation of xylose: The role of the crystal structure of the support. *Catal Sci Technol* **6**, 577–582 (2016).

75. Eaimsumang, S., Prataksanon, P., Pongstabodee, S. & Luengnaruemitchai, A. Effect of acid on the crystalline phase of TiO2 prepared by hydrothermal treatment and its application in the oxidative steam reforming of methanol. *Research on Chemical Intermediates* **46**, 1235–1254 (2020).
76. Akita, T., Okumura, M., Tanaka, K. & Tsubota, S. *Structural analyses by TEM of iridium deposited on TiO 2 powder and rutile single crystal. Journal of Electron Microscopy* vol. 53 http://jmicro.oxfordjournals.org/ (2004).
77. Reyes, P. *et al. SELECTIVE HYDROGENATION OF FURFURAL ON Ir/TiO 2 CATALYSTS. Quim. Nova* vol. 33 (2010).
78. Mohamed, Z., Dasireddy, V. D. B. C., Singh, S. & Friedrich, H. B. The mitigation of co present in the water–gas shift reformate gas over ir-tio2 and ir-zro2 catalysts. *Catalysts* **11**, (2021).
79. Siang, J. Y. *et al.* Hydrogen production from steam reforming of ethanol using a ceria-supported iridium catalyst: Effect of different ceria supports. *Int J Hydrogen Energy* **35**, 3456–3462 (2010).
80. Zieliński, M. *et al.* Studies of New Iridium Catalysts Supported on Modified Silicalite-1—Their Structure and Hydrogenating Properties. *Materials* **14**, 4465 (2021).
81. Bokhimi, X., Zanella, R. & Angeles-Chavez, C. Rutile-supported Ir, Au, and Ir-Au catalysts for CO oxidation. *Journal of Physical Chemistry C* **114**, 14101–14109 (2010).
82. Hadjiivanov, K., Lamotte, J. & Lavalley, J.-C. *FTIR Study of Low-Temperature CO Adsorption on Pure and Ammonia-Precovered TiO 2 (Anatase).* (1997).
83. Yates, J. T. & Kolasinski, K. Infrared spectroscopic investigation of the rhodium gem-dicarbonyl surface species. *J Chem Phys* **79**, 1026–1030 (1983).
84. Goellner, J. F., Guzman, J. & Gates, B. C. Synthesis and structure of tetrairidium clusters on TiO2 powder: Characterization by infrared and extended X-ray absorption fine structure spectroscopies. *Journal of Physical Chemistry B* **106**, 1229–1238 (2002).
85. Rojas, H. *et al.* Citral hydrogenation over Ir/TiO2 and Ir/TiO2/SiO2 catalysts. *Catal Today* **133–135**, 699–705 (2008).
86. Jia, A. *et al.* The effects of TiO2 crystal-plane-dependent Ir-TiOx interactions on the selective hydrogenation of crotonaldehyde over Ir/TiO2 catalysts. *Chinese Journal of Catalysis* **42**, 1742–1754 (2021).